LRP 377/89 MAY 1989

A NONLOCAL ANALYSIS OF ELECTROSTATIC WAVES IN HOT INHOMOGENEOUS BOUNDED PLASMAS

O. Sauter, J. Vaclavik and F. Skiff

A nonlocal analysis of electrostatic waves in hot inhomogeneous bounded plasmas

O. Sauter, J. Vaclavik, and F.Skiff [a)]

Centre de Recherches en Physique des Plasmas
Association Euratom - Confédération Suisse
Ecole Polytechnique Fédérale de Lausanne
21, Av. des Bains, CH-1007 Lausanne - Switzerland

ABSTRACT

A second order integro-differential equation that describes electrostatic waves in a slab plasma is solved in its full form. No expansion in the smallness of the ion Larmor radius is made. The plasma may have arbitrary density and temperature profiles and is immersed in a non-uniform magnetic field. Only small magnetic field gradients, Maxwellian equilibrium distribution functions, and $k_y = 0$ are assumed. First the integral equation is derived in Fourier space using the linearized Vlasov and Poisson equations,then it is transformed back into real space, which enables us to treat the case of bounded plasmas. The two boundary conditions specified simulate an antenna at one end of the plasma and wave-reflecting walls. Solutions having wavelengths smaller than the ion Larmor radius have been found. Comparison with experiments where ion Berstein waves are launched in argon and barium plasmas shows very good agreement with the solution of our code SEAL. We also derive and compute a positive-definite formula for the local power absorption.

---

a) Present address: Laboratory for Plasma Research, University of Maryland, College Park, MD 20742.

I. INTRODUCTION

Linear electromagnetic wave equations, especially in the Ion Cyclotron Range of Frequencies (ICRF), have been thoroughly studied using first cold and then warm plasma models. In 2-D, toroidal geometry, warm plasma codes with an expansion in the ion Larmor radius up to the second order are now available.[1,2,3] They generally assume zero electron mass (except for Ref. 1) and use a finite element method in the radial direction and a Fourier decomposition in the poloidal direction. One of the purposes of such codes is to find out how the conversion mechanism occurs and how or where the ion Bernstein wave (IBW) propagates. The latter question is hard to answer in 2-D geometry, due to resolution problems. In 1-D geometry, one can hope to have enough grid points to resolve such small wavelengths. Codes solving the full sixth order wave equation exist,[4,5,6] but the form of the dielectric tensor operator is rather complicated.[7] They can solve many interesting cases but when the wavelength of the IBW becomes comparable with the ion Larmor radius, the second order expansion in the ion Larmor radius breaks down and one obtains large spurious and unphysical modes. These spurious modes exist due to the FLR expansion. Indeed the wave equation, in its complete integral form, is equivalent to an infinite order differential equation. However, an exact solution contains only a few modes; therefore an expansion to an order greater than the number of modes introduces spurious modes which can not always be eliminated through adequate boundary conditions. Thus to take care of this problem and to be able to solve for arbitrary wavelengths, we have to use the equation in its integral form. In this way we find all the physical modes, even if they have very short wavelengths, without introducing other modes. The integral equation has already been solved in Fourier space, that is assuming an infinite extension of the plasma. Eigenvalues

and eigenvectors have been found for various cases, but always using Gaussian density profiles of the guiding centers and homogeneous temperature profiles.[8,9,10]

Let us note that the IBW are not only important in the mode conversion mechanism but also in heating processes via direct launching.[11,12]

In this paper we shall restrict ourselves to the electrostatic approximation and slab geometry with the magnetic field parallel to the z axis and the inhomogeneity along the x axis. The Vlasov and Poisson equations lead us, after linearization, to solving a homogeneous second order integro-differential equation. We shall present here the results of the **SEAL** code, which find the **S**olution of an **E**lectrostatic wave problem valid to **A**ll orders in the ion **L**armor radius, for arbitrary density, temperature and magnetic field profiles, assuming a Maxwellian equilibrium distribution function, a slowly varying magnetic field, and $k_y = 0$.

In Sec. II, the physical model as well as the basic equations are presented. Then the numerical model is developed in Sec. III and the results are shown in Sec. IV. The latter is divided into two parts : the first one gives a comparison between the results of the **SEAL** code and the local dispersion relation, while the second one gives a comparison with an experiment. In Sec. V we show how one can define a positive-definite local power absorption and present some results. Finally we draw conclusions in Sec. VI.

II. PHYSICAL MODEL

We start from the Vlasov equation within the electrostatic approximation:

$$\left(\frac{\partial}{\partial t} + \mathbf{v}\cdot\nabla\right) f_\sigma(\mathbf{r},\mathbf{v},t) = \frac{q_\sigma}{m_\sigma}\,\nabla\Phi\cdot\frac{\partial}{\partial \mathbf{v}} f_\sigma - \frac{q_\sigma}{m_\sigma}(\mathbf{v}\times\mathbf{B}_0)\cdot\frac{\partial}{\partial \mathbf{v}} f_\sigma \quad , \tag{1}$$

where σ stands for the electron or ion species, $f_\sigma(\mathbf{r},\mathbf{v},t)$ is the distribution function, $\Phi(\mathbf{r},t)$ is the fluctuating electrostatic potential and q_σ, m_σ are the charge and mass of the particles respectively. The magnetic field $\mathbf{B}_0$ is assumed to be slowly varying, which enables us to take it locally uniform. Following the conventional procedure to linearize the equation, we assume a small perturbation around the equilibrium and keep only the first order terms :

$$f_\sigma = f_\sigma^{(0)} + f_\sigma^{(1)} \quad , \quad \text{with} \quad \left|f_\sigma^{(1)}\right| << \left|f_\sigma^{(0)}\right| \quad ,$$

$$\Phi = \Phi^{(1)} \quad .$$

The equations for $f_\sigma^{(0)}$ and $f_\sigma^{(1)}$ are then :

$$\mathbf{v}\cdot\nabla f_\sigma^{(0)} + \frac{q_\sigma}{m_\sigma}(\mathbf{v}\times\mathbf{B}_0)\cdot\frac{\partial}{\partial \mathbf{v}} f_\sigma^{(0)} = 0 \quad , \tag{2}$$

$$\left(\frac{\partial}{\partial t} + \mathbf{v}\cdot\nabla\right) f_\sigma^{(1)} + \frac{q_\sigma}{m_\sigma}(\mathbf{v}\times\mathbf{B}_0)\cdot\frac{\partial}{\partial \mathbf{v}} f_\sigma^{(1)} = \frac{q_\sigma}{m_\sigma}\,\nabla\Phi\cdot\frac{\partial}{\partial \mathbf{v}} f_\sigma^{(0)} \quad . \tag{3}$$

Equation (2) is satisfied if $f_\sigma^{(0)}$ has the following form :

$$f_\sigma^{(0)} = f_\sigma^{(0)}(v_\perp, v_{//}, X = x + v_y/\omega_{c\sigma}, Y = y - v_x/\omega_{c\sigma}) \quad , \tag{4}$$

i.e. if $f_\sigma^{(0)}$ is the distribution function of the guiding centers. $\omega_{c\sigma} = q_\sigma B_0/m_\sigma$ is the cyclotron frequency. The Fourier transform of Eq. (4) gives :

$$\text{F.T.}\{ f_\sigma^{(0)}(v_\perp, v_{//}, x+v_y/\omega_{c\sigma}, y-v_x/\omega_{c\sigma})\} = f_\sigma^{(0)}(v_\perp, v_{//}, k_\perp) \exp\left(i \frac{\mathbf{k}_\perp \times \mathbf{v}_\perp}{\omega_{c\sigma}} \right) , \quad (5)$$

where the Fourier transform is defined by :

$$g(\mathbf{x}, t) = \int d^3\mathbf{k} \int d\omega\, g(\mathbf{k}, \omega)\, e^{i(\mathbf{k}\cdot\mathbf{x} - \omega t)} . \quad (6)$$

Taking the Fourier transform of Eq. (3) and using Eq. (5), one obtains the solution for $f_\sigma^{(1)}$ in the form :[13]

$$f_\sigma^{(1)}(\mathbf{k},\mathbf{v},\omega) = -\frac{q_\sigma}{m_\sigma} \sum_{j,n,p} \frac{\exp[i(\alpha-\varphi)(j-n)]}{\omega - k_{//}v_{//} - n\omega_{c\sigma}} J_j\left(\frac{k_\perp v_\perp}{\omega_{c\sigma}}\right) J_{n+p}\left(\frac{k_\perp v_\perp}{\omega_{c\sigma}}\right)$$

$$\times \int d^2\mathbf{k}'_\perp \Phi(\mathbf{k}_\perp - \mathbf{k}'_\perp, k_{//}, \omega) \exp[ip(\varphi-\varphi')]\, J_p\left(\frac{k'_\perp v_\perp}{\omega_{c\sigma}}\right) \quad (7)$$

$$\times \left[k_{//} \frac{\partial}{\partial v_{//}} + \frac{n\omega_{c\sigma}}{v_\perp} \frac{\partial}{\partial v_\perp} - i \frac{(\mathbf{k}_\perp \times \mathbf{k}'_\perp)_{//}}{\omega_{c\sigma}} \right] f_\sigma^{(0)}(\mathbf{k}'_\perp, v_{//}, v_\perp) ,$$

where J_m is the Bessel function of order m. We have introduced a small positive imaginary part in ω, i.e. $\omega = \omega_r + i\varepsilon$, such that $f_\sigma^{(1)}$ is well defined around $k_{//}v_{//} = \omega - n\omega_{c\sigma}$. The fact that ε has to be positive comes from the term $e^{-i\omega t}$ in $\Phi(x,t)$, which gives a $e^{\varepsilon t}$ dependence. Therefore, ε positive means that we " turn on " the field smoothly from $t = -\infty$. The cylindrical coordinates for $\mathbf{k}$, $\mathbf{v}$ and $\mathbf{k}'_\perp$ are defined by :

$$\mathbf{v} = (v_\perp, \alpha, v_{//}) \;\; ; \;\; \mathbf{k} = (k_\perp, \varphi, k_{//}) \;\; ; \;\; \mathbf{k}'_\perp = (k'_\perp, \varphi') \quad .$$

Closure of the equation is obtained through Poisson equation in Fourier space :

$$\mathbf{k}^2 \Phi(\mathbf{k},\omega) = \sum_\sigma \frac{q_\sigma}{\varepsilon_0} \int f_\sigma^{(1)}(\mathbf{k},\mathbf{v},\omega)\, d^3\mathbf{v} \quad . \tag{8}$$

At this point we shall take $k_y = 0$ and choose the velocity dependence of $f_\sigma^{(0)}$ as :

$$f_\sigma^{(0)}(X, v_\perp, v_{//}) = \pi^{-3/2} \frac{n_\sigma(X)}{v_{T\sigma}^3(X)} \exp\{-\frac{v_\perp^2 + v_{//}^2}{v_{T\sigma}^2(X)}\} \quad , \tag{9}$$

i.e. the equilibrium distribution function of the guiding centers, X , is assumed to be Maxwellian in velocity, with arbitrary density and temperature profiles. The quantities n_σ , T_σ and $v^2{}_{T\sigma}(x) = 2T_\sigma(x)/m_\sigma$ are the density, temperature and thermal velocity of species σ, respectively. Thus $f_\sigma^{(0)}(v_\perp, v_{//}, \mathbf{k}_\perp)$ in Eq. (5) is given by :

$$f_\sigma^{(0)}(v_\perp, v_{//}, \mathbf{k}_\perp) = f_\sigma^{(0)}(v_\perp, v_{//}, k_x) = \frac{1}{2\pi^{5/2}} \int dx'' \frac{n_\sigma(x'')}{v_{T\sigma}^3(x'')} \exp\{-\frac{v_\perp^2 + v_{//}^2}{v_{T\sigma}^2(x'')}\} e^{-ik_x x''}. \tag{10}$$

Inserting Eq. (10) into (7), we can perform the velocity integrations in Eq. (8) using the following formulas for the Bessel functions J_n and I_n :[14]

$$\sum_j J_{m\mp j}(a)\, J_j(b) = J_m(a \pm b) \quad , \tag{11a}$$

$$\int_0^\infty t\, dt\, J_n(\alpha t) J_n(\beta t) e^{\mu^2 t} = \frac{1}{2\mu^2} \exp\{-\frac{\alpha^2 + \beta^2}{4\mu^2}\} I_n(\frac{\alpha\beta}{2\mu^2}) \quad . \tag{11b}$$

The integral equation in Fourier space for $\Phi(k_x)$, assuming arbitrary

inhomogeneous density and temperature profiles, is then given by :

$$(k_x^2 + k_{//}^2)\ \Phi(k_x) + \int \mathbf{K}(k_x, k'_x)\ \Phi(k'_x)\, dk'_x = 0 \qquad (12)$$

with

$$K(k_x, k'_x) = \sum_\sigma \sum_n \frac{q_\sigma^2}{2\pi\varepsilon_0} \int dx'' \frac{n_\sigma(x'')}{T_\sigma(x'')} \left[1 + \frac{\omega}{k_{//} v_{T\sigma}(x'')} Z_{n\sigma}(x'')\right] I_n\left(\rho_\sigma^2(x'')\, k_x\, k'_x\right)$$
$$\times \exp\left\{-\frac{1}{2}\rho_\sigma^2(x'')\,(k_x^2 + k'^2_x)\right\}\ e^{-i(k_x - k'_x)x''} \quad ,$$

where $Z_{n\sigma} = Z\{(\omega - n\omega_{c\sigma}) / |k_{//}| v_{T\sigma}\}$ is the plasma dispersion function[15] and $\rho^2_\sigma = v^2_{T\sigma}/2\omega^2_{c\sigma}$ is the Larmor radius squared.

As we want to solve (12) in a bounded plasma, we need to transform it back into real space. To be able to integrate exactly over k_x and k'_x , that is without cutting out any part of the spectrum, we use the following integral representation of the Bessel function I_n :[14]

$$I_n(z) = \frac{1}{\pi}\int_0^\pi e^{z\cos\theta}\cos(n\theta)\, d\theta \quad .$$

Taking the inverse Fourier transform of Eq. (12) and integrating over k_x and k'_x, we obtain :

$$-\frac{d}{dx}\left\{\left(1-\frac{\omega}{k_{//}\,v_{Te}(x)}\,Z_{0e}(x)\,\frac{\omega_{pe}^2(x)}{\omega_{ce}^2(x)}\right)\frac{d}{dx}\,\Phi(x)\right\}$$

$$+\left\{k_{//}^2+\frac{1+\frac{\omega}{k_{//}\,v_{Te}(x)}\,Z_{0e}(x)}{\lambda_{De}^2(x)}\right\}\,\Phi(x)+\int K(x,x')\,\Phi(x')\,dx' \;=\; 0\;, \tag{13}$$

with

$$K(x,x')=\frac{1}{2\pi^2}\sum_{\sigma,n}\int dx''\,\frac{\left[1+\frac{\omega}{k_{//}\,v_{T\sigma}(x'')}\,Z_{n\sigma}(x'')\right]}{\lambda_{D\sigma}^2(x'')\,\rho_\sigma^2(x'')}\int_0^\pi d\theta\,\frac{\cos(n\theta)}{\sin\theta}$$

$$\times\exp\left\{-\frac{(x-x')^2\,(1+\cos\theta)}{4\,\rho_\sigma^2(x'')\sin^2\theta}\right\}\;\exp\left\{-\frac{\left(x''-\frac{x+x'}{2}\right)^2(1-\cos\theta)}{\rho_\sigma^2(x'')\sin^2\theta}\right\}\;,$$

where we have expanded the electron contribution to the kernel up to the second order in the electron Larmor radius. Thus, in Eq. (13) and for the rest of the paper, the subscript e stands for electrons and σ only for the ion species. $\lambda^2_{D\sigma}=\varepsilon_0 T_\sigma/n_\sigma q^2_\sigma$ is the Debye length squared.

We still need two boundary conditions to complete the second order integro-differential equation (13). We shall take them as follows :

$$\frac{d\Phi}{dx}(x_{pl}) \;=\; 0\;,$$

$$\frac{d\Phi}{dx}(x_{pr}) \;=\; -1\;, \tag{14}$$

where x_{pl} and x_{pr} are the left and right boundaries of the x interval. We shall discuss more about the boundary conditions and the limits of integration of x, or x', and x" variables in sec. IV, where we shall show that conditions (14) simulate an antenna on the right-hand side and reflecting boundaries for the field.

Let us study closer the kernel K(x,x'). We see that it is symmetric and that the integrand has two singular points at :

$$\begin{array}{llll} \text{a)} & \theta = 0 & \text{and} & x=x' \,, \\ \text{b)} & \theta = \pi & \text{and} & x''=(x+x')/2 \,. \end{array} \qquad (15)$$

At these points the integrand is proportional to $1/\sin\theta$. These singularities give a global behavior for the kernel of the form :

$$K(x,x') \sim \ln |x-x'| \,,$$

which is an integrable singularity. Therefore (13) is regular and we can expect to find a regular solution $\Phi(x)$. Note, nevertheless, that it is difficult to integrate numerically these $1/\sin\theta$ singularities to get the $\ln |x-x'|$ behavior. Thus we shall resolve these singularities using analytical integrations. This will be explained in the next section together with the numerical method used to solve (13).

III. NUMERICAL METHOD

As one of the main characteristics of the solution $\Phi(x)$ is the fact that short and long wavelengths may coexist, we shall use the finite element method to solve Eq. (13), which enables us to pack the mesh where it is needed. We shall take linear basis functions (Fig. 1), as they are the simplest for a second order equation.

Let us rewrite Eq. (13) in a more compact form :

$$-\frac{d}{dx}\left(A(x)\,\frac{d}{dx}\Phi(x)\right) + B(x)\,\Phi(x) + \int_{x_{pl}}^{x_{pr}} K(x,x')\,\Phi(x')\,dx' = 0 \quad , \tag{16}$$

where A and B can be identified from Eq. (13). The finite element method consists in solving the weak form, also called variational form, of Eq. (16). This form is obtained by multiplying (16) by a test function, $\Psi(x)$, and integrating over the plasma "volume" :

$$\begin{aligned} -\Psi(x)\,A(x)\,\frac{d}{dx}\Phi(x)\Big]_{x_{pl}}^{x_{pr}} + \int \left[\frac{d}{dx}\Psi(x)\right] A(x) \left[\frac{d}{dx}\Phi(x)\right] dx \\ + \int \Psi(x)\,B(x)\,\Phi(x)\,dx + \int dx\,\Psi(x) \int K(x,x')\,\Phi(x')\,dx' = 0 \quad , \end{aligned} \tag{17}$$

where the limits of integration have been omitted for simplicity. In this form the boundary conditions, Eq. (14), can be introduced naturally. Of course, arbitrary boundary conditions involving Φ and $d\Phi/dx$ can also be specified. It can easily be shown that the solutions of Eq. (17) are the solutions of (16) and vice versa. We then define linearly-independent basis functions $\eta_1(x)$, $\eta_2(x)$,..., $\eta_{N+1}(x)$ and solve Eq. (17) in the space spanned by $\eta_i(x)$. As mentioned above, we shall use linear basis functions defined as follows (Fig.1) :

$$\eta_i(x) = \begin{cases} \dfrac{x - x_{i-1}}{x_i - x_{i-1}} & \text{if } x_{i-1} \le x \le x_i \\ \dfrac{x_{i+1} - x}{x_{i+1} - x_i} & \text{if } x_i \le x \le x_{i+1} \\ 0 & \text{otherwise} \end{cases} \quad . \tag{18}$$

We then write $\Phi(x) = \Sigma\, u_j\, \eta_j(x)$ and introduce it into (17), while using as a test function $\Psi(x)$ the different basis functions $\eta_i(x)$. It gives :

$$\sum_j M_{ij}\, u_j \equiv \sum_j u_j \left\{ \int dx \left[\frac{d}{dx}\eta_i(x)\right] A(x) \left[\frac{d}{dx}\eta_j(x)\right] + \int dx\, \eta_i(x)\, B(x)\, \eta_j(x) + \int dx \int dx'\, \eta_i(x)\, K(x,x')\, \eta_j(x') \right\} = \eta_i(x)\, A(x)\, \frac{d}{dx}\Phi(x) \Big]_{x_{pl}}^{x_{pr}} \quad . \tag{19}$$

Therefore, to solve Eq. (17), we have to compute the matrix M_{ij} and then solve for u_j. We see clearly that an arbitrarily spaced mesh can be used easily.

The most difficult and time-consuming part is the computation of the kernel contribution K_{ij} to the matrix M_{ij}, given by :

$$K_{ij} = \int_{x_{i-1}}^{x_{i+1}} dx\, \eta_i(x) \int_{x_{j-1}}^{x_{j+1}} dx'\, K(x,x')\, \eta_j(x') \quad . \tag{20}$$

As noted above, the main problem lies in the singularities of the θ-integrand of $K(x,x')$. In order to get rid of them we need to do some analytical integrations or adequate changes of variables. Let us first show how we can eliminate these singularities through two changes of the variables x" and x', thereby proving that K_{ij} is regular. First, we change x" to :

$$z = (x'' - \frac{x + x'}{2}) \frac{\sqrt{1 - \cos\theta}}{\sin\theta} \quad ,$$

which gives for K(x,x'), Eq. (13) :

$$K(x,x') = \frac{1}{2\pi^2} \sum_{\sigma} \sum_{n} \int_0^{\pi} d\theta \, \frac{\cos(n\theta)}{\sqrt{1 - \cos\theta}} \int_{z_{pl}}^{z_{pr}} dz \exp\left\{ - \frac{z^2}{\rho_\sigma^2[x''(z)]} \right\}$$

$$\times \; C[x''(z)] \; \exp\left\{ - \frac{(x-x')^2 (1 + \cos\theta)}{4 \rho_\sigma^2[x''(z)] \sin^2\theta} \right\} \quad ,$$

with

$$z_\nu = (x_\nu - \frac{x + x'}{2}) \frac{\sqrt{1 - \cos\theta}}{\sin\theta} \quad , \quad \nu = pl, pr \quad ,$$

$$C(x'') = \frac{(1 + \frac{\omega}{k_{//} v_{T\sigma}(x'')} Z_{n\sigma}(x''))}{\lambda_{D\sigma}^2(x'') \, \rho_\sigma^2(x'')} \quad . \qquad (21)$$

We see that the second singular point, (15b), has disappeared and is replaced by the limits of integration, z_ν , that may be infinite. But this is not a problem, owing to the term $\exp(-z^2)$. For the other singularity, (15a), we proceed in the same way :

$$y = \frac{(x' - x)\sqrt{1 + \cos\theta}}{2 \sin\theta} \quad ,$$

which gives the following contribution to K_{ij} :

$$\int_0^{\pi} d\theta \cos(n\theta) \int_{y_{j-1}}^{y_{j+1}} 2\,dy \exp\left\{-\frac{y^2}{\rho_\sigma^2[x''(z)]}\right\} \eta_j\left(x + \frac{2\sin\theta}{\sqrt{1+\cos\theta}}\,y\right)$$

$$\times \int_{b_{pl}}^{b_{pr}} dz \exp\left\{-\frac{z^2}{\rho_\sigma^2[x''(z)]}\right\} C(y') \quad ,$$

with

$$y_{j\pm1} = \frac{(x_{j\pm1} - x)\sqrt{1+\cos\theta}}{2\sin\theta} \quad ,$$

$$y' = x + \frac{y\sin\theta}{\sqrt{1+\cos\theta}} + \frac{z\sin\theta}{\sqrt{1-\cos\theta}} \quad ,$$

$$b_\nu = \left(x_\nu - x - \frac{y\sin\theta}{\sqrt{1+\cos\theta}}\right)\frac{\sqrt{1-\cos\theta}}{\sin\theta} \quad , \quad \nu = pl, pr \quad .$$

Again, owing to the term $\exp(-y^2)$, the integral is regular, eventhough the integration limits may become infinite. We now see directly that all the θ singularities have disappeared, showing that K_{ij} is regular. Note that we have used the fact that $\sin\theta$ is positive as θ lies between 0 and π.

Thus we can now compute directly K_{ij}. However, this would be very time-consuming as the intervals of integration for z and y are not fixed and may be infinite, even if they could be cut around 3 or 4. Therefore we shall discretize the x" integration in N" integrations, as follows :

$$\int_{x_{pl}}^{x_{pr}} dx'' \quad \longrightarrow \quad \sum_{k=1}^{N''} \int_{x''_k}^{x''_{k+1}} dx'' \quad .$$

Then, using the central values for the plasma parameters, i.e. setting C[x"] =

$C[(x''_k + x''_{k+1}) / 2]$, we can integrate analytically in each N'' cell. This is roughly equivalent to integrating with a trapezoidal rule, except that here we keep better the track of the x'' dependence of the integrand. In particular, for homogeneous profiles, with only one interval, i.e. N'' = 1, the integration is exact. Note also that at this point we can assume a non-uniform magnetic field as the procedure carried out in Sec. II can be done in each x'' cell where the magnetic field is assumed to be uniform. This is true only if the magnetic field is slowly varying. As can be seen from (21), the x'' or z integration gives rise to error functions of the form :[16]

$$\mathrm{erf}\left\{ z_k = (x''_k - \frac{x + x'}{2}) \frac{\sqrt{1 - \cos\theta}}{\sin\theta} \right\} = \frac{2}{\sqrt{\pi}} \int_0^{z_k} e^{-t^2} dt \quad . \tag{22}$$

This is not a severe difficulty as a very precise simple formula for error functions of real arguments exists and is vectorizable.[16] We can perform the x' integration analytically using the expression for $\eta_j(x')$, Eq. (18), and neglecting the x' dependence in (22) over each interval. We could keep the x' dependence and integrate numerically, using the above y(x') variable, but, as mentioned before, it would be much more time-consuming. Nevertheless, we have checked that both methods converge to the same solution.

Thus we are left only with the x and θ integrations, which we shall compute using the Gauss formula. In this way, K_{ij} , and therefore M_{ij} , can be computed accurately, without further assumptions. We shall note, however, that the computation of the matrix takes a lot of time as loops over the x, x', x'', and θ meshes, as well as over n and σ, are needed. To reduce this time we have coded these loops in a vectorizable way, as we have run our SEAL code on Cray

machines, i.e. Cray 1, 2 and XMP. We have also decoupled the loop over the harmonics n, by inserting the summation into the θ integrand. In this way, the sum over harmonics can be done very quickly, permitting a sum over many harmonics. The typical number of harmonics used is 21, i.e. from n = -10 to +10. The running time for the cases presented below is approximately [7.5 · N" · (N / 256)^2] seconds on a Cray 2, of which 95 % is used for the computation of K_{ij}, Eq. (20).

IV. RESULTS

The plasma geometry is shown in Fig. 1. The typical parameters used are the ones of an argon plasma with a charge number Z_i = 1, density n = 10^{17} m^{-3}, temperature T_e = 14 eV, T_i = 0.1 eV, magnetic field B_0 = 0.2 T and a parallel wavenumber $k_{//}$ = 100 m^{-1}. These parameters correspond to those used in a cylindrical experiment, where electrostatic waves are launched, with which we shall compare the results of our SEAL code. First, however, we shall run the code for a few benchmarks, comparing the wavelengths with the corresponding dispersion relation, to show that it solves Eq. (13) correctly.[17]

A. Convergence study and comparison with the dispersion relation

First we show in Fig. 2 the convergence study of the values of the real and imaginary parts of Φ at the antenna, i.e. on the right-hand side of the plasma. It clearly exhibits a convergence rate of at least $1/N^2$ for N ≥ 192. For all cases shown in this paper, we have packed N/10 points in 10 Debye lengths on the right and on the left-hand side of the plasma. The rest of the points are equally spaced in between. Therefore for N = 192 points, we have packed 19 points on each side of the

plasma, which leaves 154 points inside. As the solution has about 25 short wavelengths, we can deduce from Fig. 2 that, after having packed a few points to resolve the Debye screening, we have a good solution with 6 points per wavelength or more. To illustrate this better, we have plotted in Fig. 3a the solutions with N=160 and 192 points. If a solution with N greater than 192 was plotted on Fig. 3a, one would not be able to distinguish it from the solution with N=192 points. In Fig. 3a, we have cut the solutions at x=2.99 cm, that is near the antenna, as there is about one order of magnitude difference between the amplitude of the electrostatic potential inside the plasma and at the antenna. We show the solution near the antenna in Fig. 3b, where we have used the same units, but not the same scale, as in Fig. 3a. We see the sharp drop of the wave amplitude due to the Debye screening and that it has indeed the Debye scaling, as the Debye length is of the order of 10^{-3} cm. Let us note also that the ratio of the amplitudes at the antenna and inside the plasma is of the same order as in the experiment, where one also sees the Debye screening effect. This is a pure electrostatic shielding effect.

We have also checked the computation of the kernel by computing the electron contribution in the kernel, without using its Larmor expansion. That is, we have taken $A(x) = 1$ and $B(x) = k_{//}^2$ in Eq. (16), and σ summing over electrons and ions in K(x,x'), Eq.(13). The solution obtained is the same as the one shown in Fig.3, within 2 or 3 digits, i.e. it could not be differentiated from the other solution if they were plotted on top of each other, except for a few points near the right boundary, where the electron Larmor radius is of the same order as the wavelength.

Let us discuss shortly the boundary conditions and the limits of integration of x and x" in Eq.(13). Formally, both intervals should extend from $-\infty$ to $+\infty$, as we have transformed Eq.(12) back from Fourier space. The x" interval depends on the

density and temperature profiles of the guiding centers. We can cut this interval, named $[x''_{left}, x''_{right}]$, where the profiles vanish. On the other hand, limiting the x interval at $[x_{pl}, x_{pr}]$, consists in imposing reflecting boundaries for the field, as will be seen below. Thus, both x and x'' intervals can be chosen independently. Note that there are still some particles on the distance of a few Larmor radii outside the x'' interval due to finite Larmor radius. This is shown in Figure 4, where we have chosen $x''_{right} = -x''_{left} = 2$ cm and $x_{pr} = -x_{pl} = 3$ cm. The boundary conditions have been taken as follows :

$$\begin{aligned} \frac{d\Phi}{dx}(x_{pl}) &= 0 \quad , \\ \frac{d\Phi}{dx}(x_{pr}) &= 0 \quad , \end{aligned} \tag{23}$$

and we have introduced a source term proportionnal to $\delta(x)$ in the right-hand side of Eq.(13), where $\delta(x)$ is the Dirac function. We have computed the electron contribution inside the kernel K(x,x') in order that the coefficients A and B of Eq.(16) are continuous, and we have imposed a jump of $\Phi'(x)$ and continuity of $\Phi(x)$ at the antenna. We see in Fig.4 that both IBW and ion acoustic wave (IAW) are emitted and that they connect to an evanescent wave in the vacuum. Note, nevertheless, that the transition does not occur at 2 cm, where the guiding center profiles vanish, but at 2.2 cm, which is about two ion Larmor radii further, where the profiles of the particles vanish. If we bring the walls closer, i.e. if we shrink the x interval, the solution builds up standing waves, especially for the IAW, which shows that the finite x interval imposes reflecting boundaries for the field. Therefore, the boundary conditions (14) simulates an antenna at $x=x_{pr}$ and reflecting walls at both sides. We have verified this by introducing boundary conditions as above, Eq.(23), a source term proportionnal to $\delta(x-x_{pr})$, and by

taking the same intervals for x and x". We have obtained exactly the same solution as shown in Fig.3, except, naturally, very close to the right boundary, as $\Phi'(x_{pr})$ is not the same.

We shall now compare the results of our code with the dispersion relation. This relation is obtained in the case of an infinite and homogeneous plasma directly from Eq. (12), after integration over x" and k'_x :

$$D(k_x) = k_x^2 + k_{//}^2 + \sum_{\sigma} \sum_{n} \frac{(1 + \frac{\omega}{k_{//} v_{T\sigma}} Z_{n\sigma})}{\lambda_{D\sigma}^2} I_n(\rho_\sigma^2 k_x^2)\, e^{-\rho_\sigma^2 k_x^2} = 0 \quad . \qquad (24)$$

One sees immediately from this formula that $D(k_x)$ has no zeros for very large k_x as $I_n(x)\, e^{-x}$ is proportional to $x^{-1/2}$ for $|x| >> 1$. Therefore (24) has a finite number of real solutions, i.e. of modes. This explains why spurious modes are introduced when (24), or (12), is expanded in an infinite series of the parameter $k_x \rho_\sigma$. Figure 5 shows the dispersion relation for an argon plasma. Two modes are present : the IAW, which is not sensitive to harmonics as the ratio T_e/T_i is large, and the IBW. We have chosen these parameters because the two waves are "decoupled" and have comparable amplitudes, which allows us to precisely identify them, as can be seen in Fig. 3. In this case, the plasma is homogeneous and $\omega/\omega_{ci} = 3.50$. From the dispersion relation we obtain the following wavelengths :

$$\lambda_{\text{ion ac.}}^{\text{Disp. rel.}} = 2.45 \text{ cm} \quad , \qquad \lambda_{\text{Bernstein}}^{\text{Disp. rel.}} = 2.37 \text{ mm} \quad ,$$

whereas the wavelengths measured on the solution shown in Fig. 3 are :

$$\lambda^{sol.}_{ion\ ac.} = 2.40 \pm 0.03\ cm \quad , \qquad \lambda^{sol.}_{Bernstein} = 2.40 \pm 0.03\ mm \quad ,$$

which are in a very good agreement. Note that we do not expect to get exactly the same values, as the code calculates the solution for a bounded plasma.

We shall now compare the solution with the dispersion relation in two cases with a weak inhomogeneity. This time we solve $D(k_x) = 0$ using the local plasma parameters. First we study the case of inhomogeneous temperature profiles. As the IAW is sensitive mainly to the electron temperature and the IBW to the ion temperature, we take both profiles inhomogeneous :

$$T_\sigma(x) = \frac{T_\sigma(x_{pl}) - T_\sigma(x_{pr})}{4\,x_p^3}\,(x + x_p)^3 - 3\,\frac{T_\sigma(x_{pl}) - T_\sigma(x_{pr})}{4\,x_p^2}\,(x + x_p)^2 + T_\sigma(x_{pl}) \quad ,$$

$$x_{pr} = -\,x_{pl} = x_p = 3\ cm \quad ,$$

i.e. we take cubic profiles with zero slopes at the edges and :

$$T_e(x_{pl}) = 30\ eV \quad , \qquad T_e(x_{pr}) = 2.0\ eV \quad ,$$
$$T_i(x_{pl}) = 0.5\,eV \quad , \qquad T_i(x_{pr}) = 0.05\ eV \quad .$$

From the dispersion relation, we get the following wavelengths for both waves:

at $x = x_{pl} = -3$ cm :	$\lambda_{ion\ ac.} = 3.8$ cm	$\lambda_{Bernstein} = 6.3$ mm
$x = 0$ cm :	$\lambda_{ion\ ac.} = 2.4$ cm	$\lambda_{Bernstein} = 2.9$ mm
$x = x_{pr} = 3$ cm :	$\lambda_{ion\ ac.} = 0.9$ cm	$\lambda_{Bernstein} = 2.1$ mm .

We see in Fig. 6 that the solution follows well these values.

The second case is that of a non-uniform magnetic field. We introduce a "toroidal" profile proportional to $1/(R_0 \pm x)$, depending on whether the antenna is on the low field side (LFS) or the high field side (HFS) respectively. Note that this profile is slowly varying as assumed above. We have chosen $R_0 = 0.647$ m, such that for the HFS case $\omega/\omega_{ci} = 3.95$ at $x = x_{pl}$ and 3.60 at $x = x_{pr}$, and vice versa for the LFS case. From the dispersion relation, we expect the following wavelengths for the HFS case :

at $x = x_{pl}$, $\omega/\omega_{ci} = 3.95$: $\lambda_{ion\ ac.} = 2.1$ cm $\lambda_{Bernstein} = 4.3$ mm

$x = 0$ cm , $\omega/\omega_{ci} = 3.775$: $\lambda_{ion\ ac.} = 2.2$ cm $\lambda_{Bernstein} = 4.2$ mm

$x = x_{pr}$, $\omega/\omega_{ci} = 3.60$: $\lambda_{ion\ ac.} = 2.4$ cm $\lambda_{Bernstein} = 2.9$ mm .

The imaginary part of the solution from the SEAL code is shown in Fig. 7. We expect a strong ion cyclotron damping of the ion Bernstein wave when ω is closer to a harmonic, i.e. when ω/ω_{ci} approaches 4. This is clearly shown in Fig. 7a, where the antenna is in a region where ω is far from a harmonic. Therefore both waves are well excited, but as the waves approach the left-hand side, the cyclotron damping is enhanced and the IBW is damped. On the other hand, when the antenna is on the LFS, (Fig. 7b), i.e. in a region of a high ion cyclotron damping, only the IAW is launched. We see, however, that the IBW is re-emitted on the left boundary, but naturally with a smaller amplitude than via direct launching (Fig. 7a).

We have thus shown in this section that our code gives the right solutions for different homogeneous and weakly inhomogeneous cases, and that the convergence behaves well. We shall now compare it with the results of an

experiment performed at our institute.

B. Comparison with experiment.

In this experiment, electrostatic waves are launched in a homogeneous cylindrical plasma of 2.5 cm radius and of 5 meter length.[18] Two plasmas have been studied : the first with argon, $n \cong 10^{17}$ m^{-3}, $B_0 \cong 0.2$ T, $\omega/\omega_{ci} \cong 3.5$, $k_{//} \cong 200$ m^{-1}, $T_e \cong 18$ eV, and $T_i \cong 0.03$ eV and the second with barium, $n \cong 10^{16}$ m^{-3}, $B_0 \cong 0.25$ T, $\omega/\omega_{ci} \cong 3.07$, $k_{//} \cong 30$ m^{-1}, and $T_e = T_i \cong 0.1$ eV.

The wave electrostatic potential in the argon plasma is shown in Fig. 8a taken from Ref. 18. The corresponding numerical result is presented in Fig. 8b and shows very good agreement. This is not, however, very surprising, as in this case the solution is approximately the sum of the two modes found in solving the homogeneous Eq. (24). This is due to the high ratio T_e/T_i and the decoupling of the modes in the dispersion relation, as mentioned before.

In the case of the barium Q-plasma, however, both temperatures are equal, which changes the dispersion relation dramatically (Fig. 9). In isothermal plasmas, it is difficult to distinguish between the ion acoustic and the Bernstein branches. Another difficulty is the fact that the experimental plasma is drifting along the cylindrical axis with a non-negligible velocity v_{drift}. Therefore there is a Doppler shift of the frequency, $k_{//}\, v_{drift}$, between the plasma and laboratory frames. Thus we expect an influence of the $k_{//}$ spectrum of the antenna, as a change in $k_{//}$ changes also the effective frequency of the wave. The antenna is made of two plates at the plasma edge with oscillating charges. The parallel wavenumber is determined by the size and separations of the plates along the

magnetic field. Therefore $k_{//}$ is not uniquely defined, which is why we have computed the solutions for different $k_{//}$, introducing the Doppler shift. The sum of these solutions gives the final solution shown in Fig. 10b. We can compare it with the experimental result, Fig. 10a,[19] where we see that the wave has a very different behavior than in the case of argon. First, it seems that only one mode is present : in this case it is the IAW. Secondly, as the ion cyclotron damping is important, the wave is rather quickly damped over a few wavelengths. Figure 10 shows that both features, as well as the relative amplitudes along the wave, are well represented by the numerical result.

V. POWER ABSORPTION

We want to define the power absorbed by the particles and especially the local power absorption. The first idea is to calculate $P(x) = \mathrm{Re}\ [\ \mathbf{j}(x) \cdot \mathbf{E}^*(x)\ ]$. This definition, however, is not adequate as it takes into account the flux of energy of streaming particles. Indeed, let us consider the power absorbed in a "volume" element $P(x)dx$; then the power due to the energy flux of particles streaming in and out of this "volume" element is counted, as has been shown in Refs. 20 and 21. We shall follow the procedure of Ref. 21 in order to define a local power absorption density $P_L(x)$ that does not take the energy fluxes into account. In this way, for the case of $k_y = 0$, we shall be able to define a positive-definite local power absorption for an inhomogeneous plasma, which is valid to all orders in the Larmor radius. Of course, $P_L(x)$ is in fact the average $\langle P_L(x) \rangle$ over the length parallel to the magnetic field and over time.

From Ref. 21, $P_L(x)$ is given by :

$$P_L(x) = \mathrm{Re} \sum_\sigma \frac{i q_\sigma}{2} \int d^3v\, dk\, dk'''\, \Phi^*(k''') \left\langle (k'''v'_x + k_{//} v'_{//})\, f_\sigma^{(1)}(k,v')\, e^{i(k-k''')x'} \right\rangle_t , \quad (25)$$

where we have omitted the subscript x from the k_x variables and introduced the Fourier transform defined in Sec. II. x' and v' are the Lagrangian coordinates of the particles at the time t' as they move along an unperturbed orbit :

$$\begin{aligned} x' &= x + \frac{v_\perp}{\omega_{c\sigma}} (\sin\alpha - \sin\alpha') \quad , \\ \mathbf{v}' &= v_\perp (\cos\alpha'\, \mathbf{e}_x + \sin\alpha'\, \mathbf{e}_y) + v_{//}\, \mathbf{e}_z \quad , \\ \alpha' &= \alpha - \omega_{c\sigma}\tau \quad , \qquad \tau = t' - t \quad . \end{aligned} \quad (26)$$

Further substituting x , v' and $f_\sigma^{(1)}$, from Eqs. (26) and (7), in (25), taking the time average and using extensively Eq. (11a) and the formula :[14]

$$e^{ia\sin\theta} = \sum_n e^{in\theta} J_n(a)$$

we obtain then the following expression :

$$\begin{aligned} P_L(x) = \mathrm{Re} \sum_{\sigma,n} \frac{2\pi i q_\sigma^2}{m_\sigma} \int dv_{//} v_\perp dv_\perp \int dk \int dk''' \int dk'\; \Phi(k')\, \Phi^*(k''') \\ \times \frac{(k_{//} v_{//} + n\omega_{c\sigma})^2}{\omega - k_{//} v_{//} - n\omega_{c\sigma}} e^{ikx} f_\sigma^{(0)}(k+k'''-k')\, J_0(\eta)\, J_n(\eta''')\, J_n(\eta') \quad , \end{aligned} \quad (27)$$

with

$$\eta^v = \frac{k^v v_\perp}{\omega_{c\sigma}} \quad .$$

Note that the integration over the velocity angle α has already been performed and

that the variable k has been changed to k + k'''. In order to be able to integrate over the variables k, we use the following integral representations for the Bessel functions J_n :[14]

$$J_n(z) = \frac{i^{-n}}{\pi}\int_0^{\pi} d\theta\, e^{iz\cos\theta}\cos n\theta = \frac{i^{+n}}{\pi}\int_0^{\pi} d\theta'\, e^{-iz\cos\theta'}\cos n\theta' \quad .$$

For the first two Bessel functions in Eq. (27), we take the first formula with θ and θ''' as integration variables respectively and for the last one, the second formula with θ'. In this way, introducing the inverse Fourier transform of the electrostatic potential and of the equilibrium distribution function, Eq. (10), we can integrate over k, k', k''' to obtain :

$$P_L(x) = \mathrm{Re}\sum_{n,\sigma}\frac{2iq_\sigma^2}{\pi^{7/2}m_\sigma}\int dv_{//}v_\perp dv_\perp dx''dx'dx'''\int_0^{\pi} d\theta\, d\theta'\, d\theta'''\;\Phi(x')\,\Phi^*(x''')$$

$$\times\cos n\theta'\cos n\theta'''\;\frac{n_\sigma(x'')}{v_{T\sigma}^5(x'')}\;\exp\left\{-\frac{v_{//}^2+v_\perp^2}{v_{T\sigma}^2}\right\}\;\frac{(k_{//}v_{//}+n\omega_{c\sigma})^2}{\omega-k_{//}v_{//}-n\omega_{c\sigma}} \qquad (28)$$

$$\times\,\delta\left(x-x''+\frac{v_\perp\cos\theta}{\omega_{c\sigma}}\right)\,\delta\left(x'-x''+\frac{v_\perp\cos\theta'}{\omega_{c\sigma}}\right)\,\delta\left(x'''-x''+\frac{v_\perp\cos\theta'''}{\omega_{c\sigma}}\right) \quad ,$$

where δ(y) are Dirac distributions, with which we can easily integrate over $v_\perp$, θ' and θ''' respectively. As $v_\perp$ is positive and cos θ^v is defined between -1 and +1, we have the following conditions :

$$v_\perp = \frac{(x''-x)}{\cos\theta}\,\omega_{c\sigma} \geq 0 \quad , \qquad (29a)$$

$$-1 \leq \cos\theta^v = \frac{(x''-x^v)}{(x''-x)}\cos\theta \leq +1 \quad . \qquad (29b)$$

We still have to integrate over $v_{//}$. This is easily done using :

$$\mathrm{Re}\left\{ \lim_{\varepsilon \to 0^+} \frac{i}{\omega_r - k_{//} v_{//} - n\omega_{c\sigma} + i\varepsilon} \right\} = \pi\, \delta(\omega_r - k_{//} v_{//} - n\omega_{c\sigma}) \quad ,$$

which clearly indicates that only the resonant particles contribute to the power absorption. The final form of the local power absorption, valid for an arbitrary inhomogeneous plasma and to all orders in the Larmor radius is then given by :

$$P_L(x) = \sum_{n,\sigma} \frac{2q_\sigma^2}{\pi^{5/2} m_\sigma} \frac{\omega^2}{|k_{//}|} \int dx'' \, \frac{n_\sigma(x'')\, \omega_{c\sigma}^2(x'')}{v_{T\sigma}^5(x'')} \, \frac{e^{-\xi_{n\sigma}^2(x'')}}{|x - x''|}$$
$$\times \int_0^{\frac{\pi}{2}} d\theta \, \exp\left\{ -\frac{(x - x'')^2}{2\rho_\sigma^2 \cos\theta} \right\} \left| \int dx' \, \Phi(x') \frac{\cos[n u(x')]}{\sin[u(x')]} \right|^2 \quad , \tag{30}$$

with

$$u(x') = \begin{cases} \arccos\left(\dfrac{x'' - x'}{|x'' - x|} \cos\theta \dfrac{\omega_{c\sigma}}{|\omega_{c\sigma}|} \right) & \text{if } \dfrac{|x'' - x'|}{|x'' - x|} \cos\theta \leq 1 \\ 0 & \text{otherwise} \end{cases} \quad ,$$

$$\xi_{n\sigma}(x'') = \frac{\omega - n\omega_{c\sigma}(x'')}{k_{//}\, v_{T\sigma}(x'')} \quad .$$

Equation (30) shows that $P_L(x)$ is positive-definite, indicating that it is a good definition for the local power absorption. Moreover, it shows that in the case of $k_y = 0$, our equilibrium is stable. From $P_L(x)$ we can define the power absorbed by the particles between the antenna and the abscissa x, as follows :

$$\overline{P}_L(x) = \int_x^{x_{pr}} P_L(x')\,dx' \quad .$$

In particular, $\overline{P}_L(x_{pl})$ is the total power absorbed in the plasma.

The computation of $P_L(x)$, Eq.(30), is very time-consuming, as 3 integrals and two sums are needed for each x. Moreover, the inner integral over x' computes a function, u(x'), with values which depend on the other variables. For the electron contribution we can use the formula expanded to second order in the electron Larmor radius.[21] Note also that the number of harmonics, Nn, can be reduced to the two closer harmonics, due to the $\exp[-\xi^2_{n\sigma}]$ term. Despite this, we cannot use many points for the different integrals and $P_L(x)$ is therefore very oscillatory, especially due to the sharp Debye screening near the edge. In order to check that the oscillations are only numerical, we show in Figure 11 the local power absorption $P_L(x)$, calculated for the electrons only, in the case of the argon plasma, Fig.3. This way, we can compare it with the expanded formula, as the electron Larmor radius is very small compared to the wavelengths, except near the edge. The oscillatory curves, Fig.(11a) and (11b), represent $P_L(x)$, Eq.(30), for two different resolutions and the dotted smooth curves represent the expanded formula for $P_L(x)$. We see that if we take enough points for x, x' and x", then $P_L(x)$ is quite smooth and closely follows the expanded formula (dotted line). Note that this was only possible by taking fewer x points, NX=128, and a shorter x interval, as the computing time goes as $230 \cdot NX \cdot NX'' \cdot NX' / (128)^3$ seconds. Nevertheless, we see in Fig.12a, that the power absorption $\overline{P}_L(x)$ is well represented with a small number of points, as the oscillations are integrated out. We show in Fig.12b the total power absorption profile for the argon case, where the ion contribution has been added to that of the electrons. In this case, four times more power is absorbed by the electrons than by the ions. We see also, as expected for a standing

wave, that the power is absorbed all over the plasma. Moreover, very little power is absorbed near the antenna, eventhough the field is very large, as the Debye length is very small.

VI. CONCLUSION

We have derived the equation for the electrostatic potential in a 1-D inhomogeneous bounded plasma from the linearized Vlasov-Poisson equations, assuming $k_y = 0$, a slowly varying magnetic field, and arbitrary Maxwellian density and temperature of the guiding centers, but without approximations on the size of the Larmor radius. We have checked the solution obtained with the code SEAL, solving this equation for a few benchmarks. The solution has a good convergence rate and the wavelengths agree well with the local dispersion relation, even for wavelengths smaller than the Larmor radius. The solution has also been compared to the waves measured in two experiments, in argon and barium plasmas, made at our institute.

We have also derived a positive-definite local power absorption formula valid to all orders in Larmor radius, in a 1-D inhomogeneous plasma, and assuming $k_y = 0$. This local power absorption can be computed for each species and has been compared with the formula expanded to second order in Larmor radius for the electrons.

ACKNOWLEDGEMENTS

The authors would like to thank Dr. F. Anderegg and Dr. T. M. Good for their collaboration and for providing us experimental results shown in this paper.

This work was partly supported by the Swiss National Science Foundation.

REFERENCES

1 A. Fukuyama, K. Itoh, and S.-I. Itoh, Comput. Phys. Rep. 4, 137 (1986).

2 D. Edery and H. Picq, Comput. Phys. Commun. 40, 95 (1986).

3 M. Brambilla and T. Krücken, Nucl. Fusion 28, 1813 (1988).

4 F. Skiff, M. Ono, P. Colestock, and K.L. Wong, Phys. Fluids 28, 2453 (1985), and Phys. Fluids 31, 2030 (1988).

5 K. Appert, T. Hellsten, H. Lütjens, O. Sauter, J. Vaclavik, and L. Villard, in Proceedings of the International Conference on Plasma Physics, Kiev, Invited Papers, edited by A.G. Sitenko (World Scientific, Singapore, 1987), p. 1230.

6 E.F. Jaeger, D.B. Batchelor, and H. Weitzner, Nucl. Fusion 28, 53 (1988).

7 Th. Martin and J. Vaclavik, Helv. Phys. Acta 60, 471 (1987).

8 H. Sanuki, T. Watanabe, and M. Watanabe, Phys. Fluids 23, 158 (1980).

9 R. Marchand, C.F. Zhang, and Y.C. Lee, Phys. Fluids 26, 195 (1983).

10 R.D. Ferraro, R.G. Littlejohn, H. Sanuki, and B.D. Fried, Phys. Fluids 30, 1115 (1987).

11 M. Ono, P. Beiersdorfer, R. Bell, S. Bernabai, A. Cavallo, A. Chmyga, S. Cohen, P. Colestock, G. Gammel, G.J. Greene, J. Hosea, R. Kaita, I. Lehrman, G. Mazzitelli, E. Mazzucato, D. McNeill, K. Sato, J. Stevens, J. Timberlake, J.R. Wilson, and A. Wouters, Phys. Rev. Lett. 60, 294 (1988).

12 J.D. Moody, M. Porkolab, C.L. Fiore, F.S. McDermott, Y. Takase, J. Terry, and S.M. Wolfe, Phys. Rev. Lett. 60, 298 (1988).

13 F. Yasseen and J. Vaclavik, Phys. Fluids 26, 468 (1983).

14 I.S. Gradshteyn and I.M. Ryzhik, Tables of Integrals, Series, and Products (Academic, New York, 1965).

15 B.D. Fried and S.D. Conte, The Plasma Dispersion Function (Academic, New York, 1961).

16 Handbook of Mathematical Functions, edited by M. Abramowitz and I.E. Stegun (National Bureau of Standards, Washington, DC, 1964).

17 O. Sauter and J. Vaclavik, Europhys. Conf. Abstr. 12B, Part II, 758 (1988).

18 F. Skiff, F. Anderegg, M.Q. Tran, P.J. Paris, T.N. Good, R.A. Stern, and N. Rynn, in Proceedings of the International Conference on Plasma Physics, Kiev, Invited Papers, edited by A.G. Sitenko (World Scientific, Singapore, 1987), p. 441, and Contributed Papers (Naukova Dumka, Kiev, 1987), Vol. 1, p. 55.

19 F. Anderegg, and T.N. Good (private communication).

20 B.D. McVey, R.S. Sund, and J.E. Scharer, Phys. Rev. Lett. 55, 507 (1985).

21 J. Vaclavik and K. Appert, Plasma Phys. Controlled Fusion 29, 257 (1987).

Figure captions

Figure 1 : Plasma geometry with a non equidistant mesh with N intervals. Plasma left and right boundaries are at $x = x_{pl}$ and $x = x_{pr}$, respectively. $\eta_i(x)$ is the linear basis function of the node x_i.

Figure 2 : Convergence study of the real (triangles) and imaginary (circles) parts of $\Phi(x_{pr})$ versus $1 / N^2$. A few values of N are pointed out on the lower x-axis.

Figure 3 : Real part of the solution $\Phi(x)$ for a homogeneous argon plasma with $T_e = 14$ eV, $T_i = 0.1$ eV, $B_0 = 0.2$ T, $k_{//} = 100$ m^{-1}, $n = 10^{17}$ m^{-3}, and $\omega/\omega_{ci} = 3.50$. Two meshes have been used : N = 160 (dashed line) and N = 192 (solid line). The antenna is at x = 3 cm. Figure 3a shows the solutions between x_{pl} and 2.99 cm, and Fig.3b near the antenna (only with N = 192). The same units, but not the same scales, have been used for both plots.

Figure 4 : Real part of solution $\Phi(x)$ for the same plasma parameters as in Fig.3, but with the antenna at x=0 and with the guiding center interval [x''_{left} , x''_{right}] shortened to [-2 , +2] cm. That is, guiding center density and temperatures are set to zero outside this interval.

Figure 5 : Dispersion relation of an argon plasma with the same parameters as in Fig.3. In this case, $\rho_i \cong 1$ mm.

Figure 6 : Imaginary part of solution $\Phi(x)$ for an argon plasma with the same parameters as in Fig.3, but with inhomogeneous temperature profiles. $T_e(x)$ and $T_i(x)$ are cubics with zero slopes at edges.

Figure 7 : Imaginary part of solution $\Phi(x)$ for an argon plasma with the same parameters as in Fig.3, but with a non-uniform magnetic field. $B_0(x)$ is proportionnal to $1 / (R_0 \pm x)$, depending on whether the antenna, at $x = x_{pr}$, is on the LFS or the HFS respectively. $R_0 = 64.7$ cm was chosen such that $\omega/\omega_{ci}(x_{pl}) = 3.95$ and $\omega/\omega_{ci}(x_{pr}) = 3.60$ in Fig.7a, and vice-versa in Fig.7b.

Figure 8 : Experimental and numerical electrostatic potential in an argon plasma. The parameters used for the numerical simulation are the following : $T_e = 18$ eV, $T_i = 0.03$ eV, $B_0 = 0.2$ T, $k_{//} = 200$ m^{-1}, $n = 10^{17}$ m^{-3}, and $\omega/\omega_{ci} = 3.50$.

Figure 9 : Dispersion relation of a barium plasma with $B_0 = 0.25$ T, $k_{//} = 30$ m^{-1}, $T_e = T_i = 0.1$ eV, $n = 10^{16}$ m^{-3}. In this case, $\rho_i \cong 1.5$ mm.

Figure 10 : Experimental and numerical electrostatic potential in a barium plasma. The parameters used for the numerical simulation are the same as in Fig.9. The solutions with $k_{//} = 25$, 26, 27, 28, 29, and 30 m^{-1} have been summed. A frequency equal to $2.6\,\omega_{ci}$ in the laboratory frame and a drift velocity $v_{drift} / \omega_{ci} = 0.016$ m have been used. Therefore the frequency in the plasma frame is defined by : $\omega/\omega_{ci} = 2.60 + 0.016 \cdot k_{//}$, and is around 3.05.

Figure 11 : Local power absorption density $P_L(x)$, for the electrons only, with the same plasma parameters as in Fig.3, but with $x_{pr} = -x_{pl} = 1$ cm. The solid lines correspond to $P_L(x)$ and the dotted lines to the expansion formula. Two sets of meshes for x, x' and x" have been used :
(a) N=128, N'=N"=64, which took 67 seconds of computing time, and
(b) N=320, N'= N"=160, which took 837 seconds.

Figure 12 : (a) $\overline{P}_L(x)$, Local power absorption integrated between x and x_{pr}, for electrons only. The same parameters as in Fig.11 have been used, with low (dashed line) and high (solid line) resolution.
(b) $\overline{P}_L(x)$ computed for ions (dotted line) and electrons (dashed line) using the higher resolution, as in Fig.11b. The solid line represents the total power absorbed by the plasma between x and the antenna.

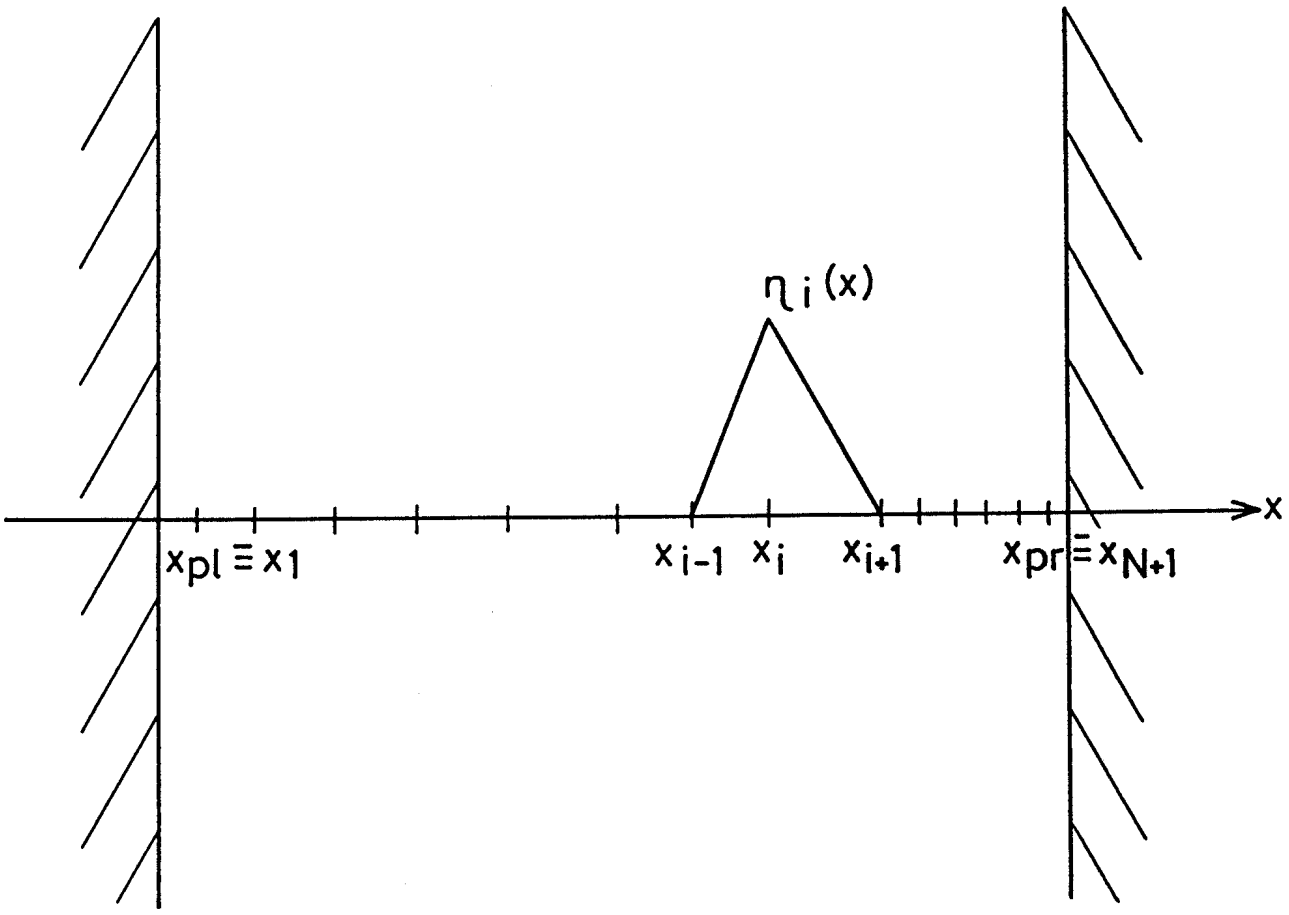

Figure 1.

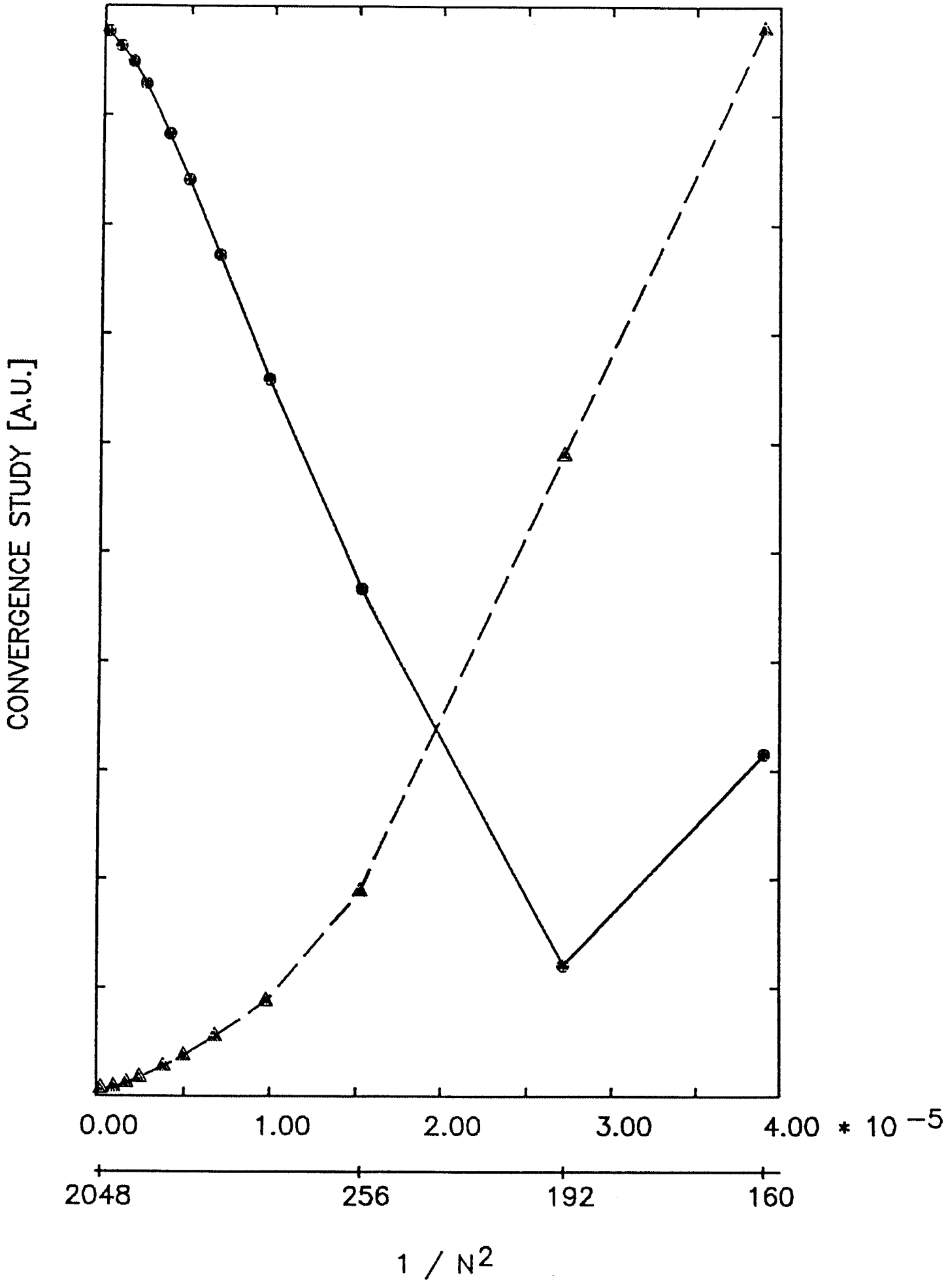
CONVERGENCE STUDY [A.U.]
0.00
1.00
2.00
3.00
4.00 * 10 −5
2048
256
192
160
1 / N2

Figure 2.

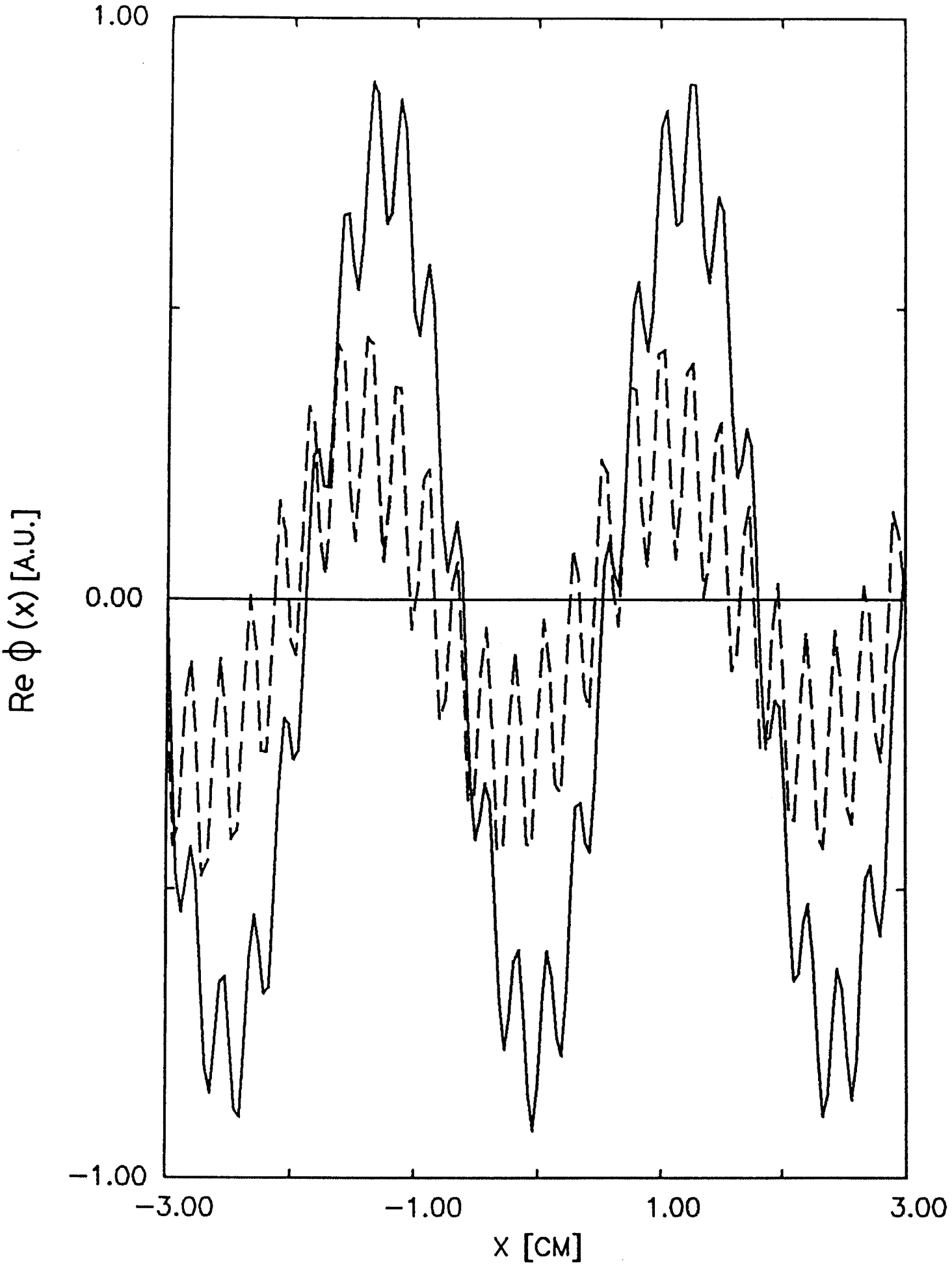

Figure 3a.

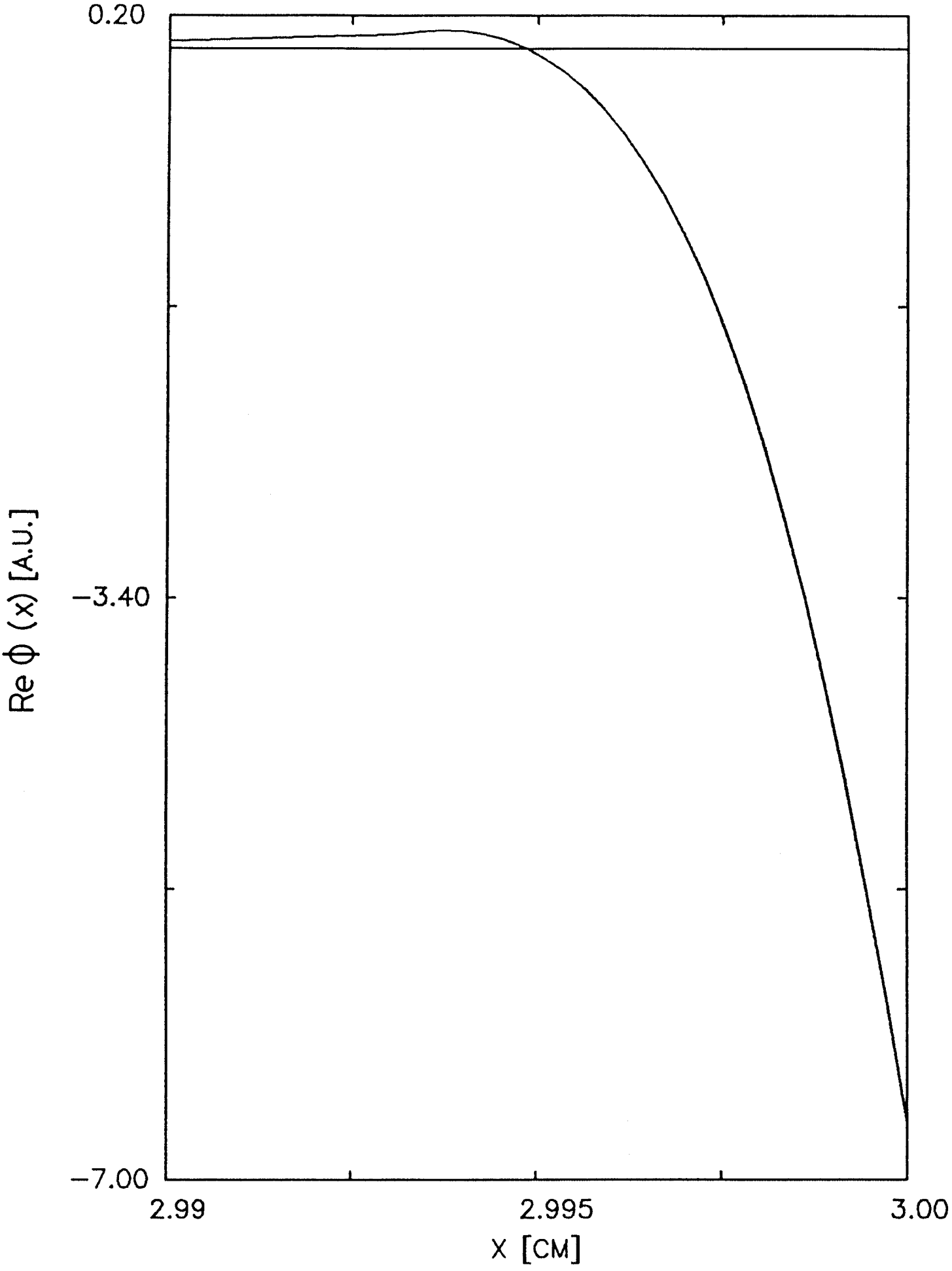

Figure3b.

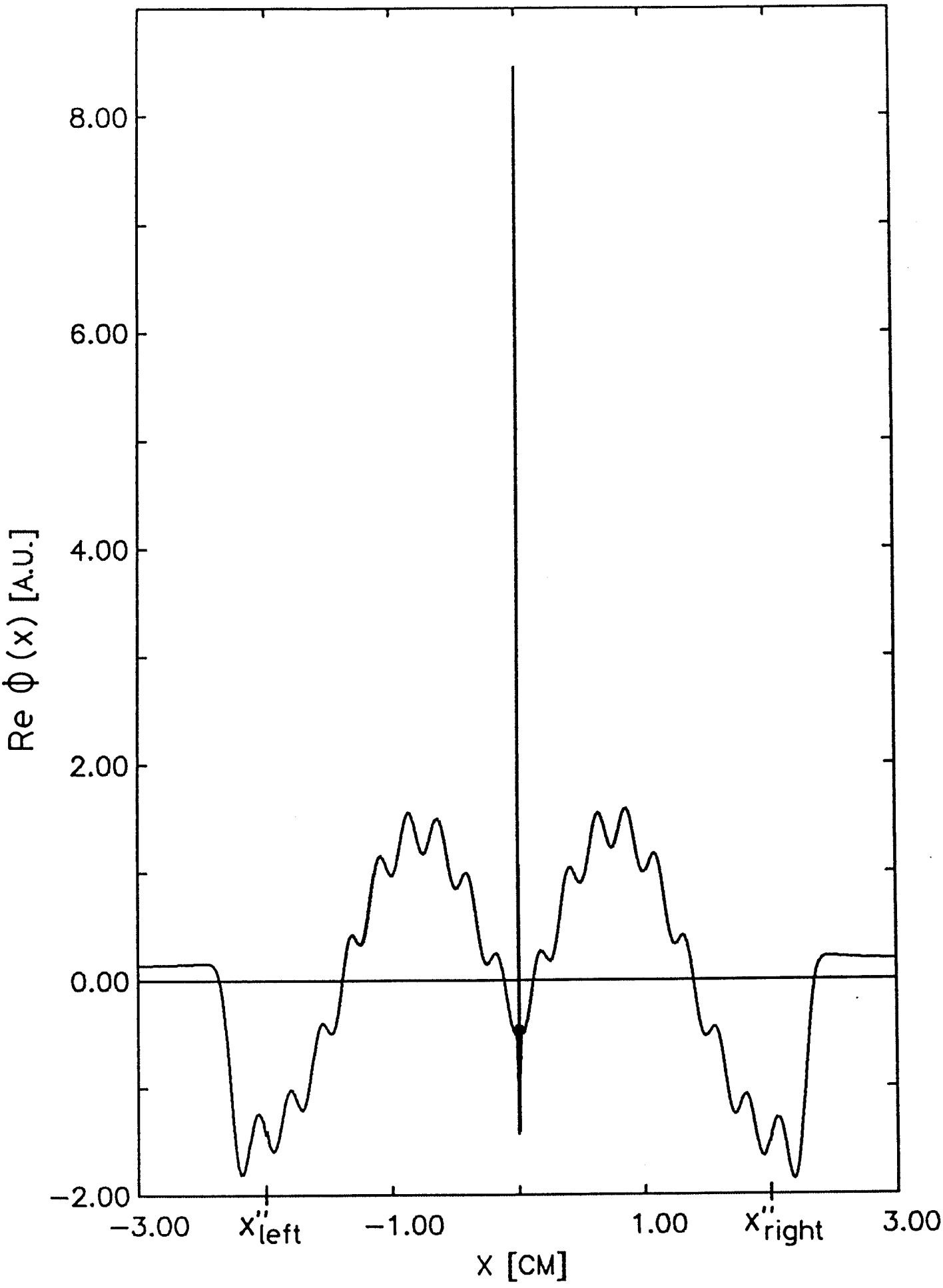
8.00
6.00
4.00
2.00
0.00
−2.00
Re Φ (x) [A.U.]
−3.00
x''left
−1.00
1.00
x''right
3.00
X [CM]

Figure 4.

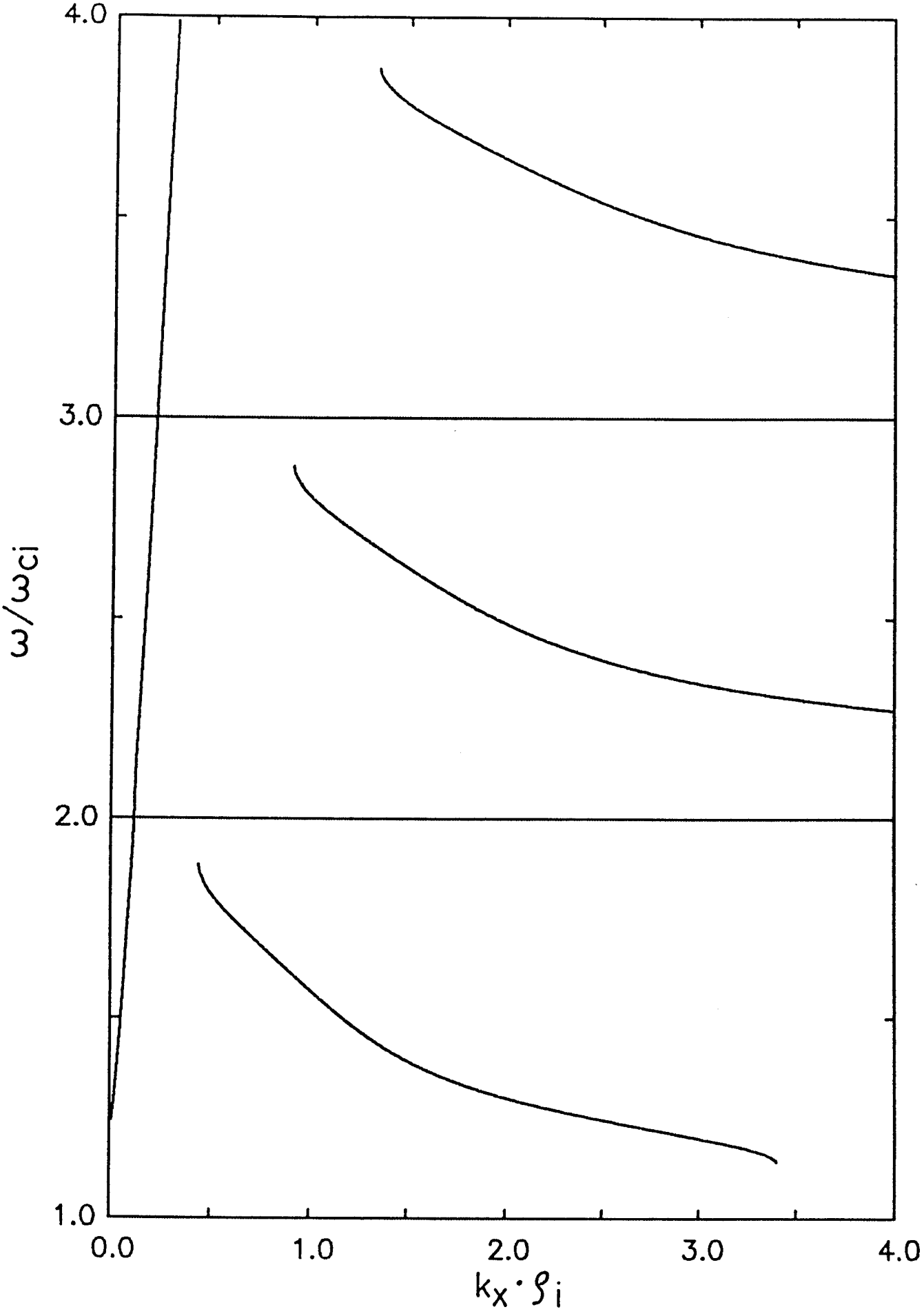

Figure 5.

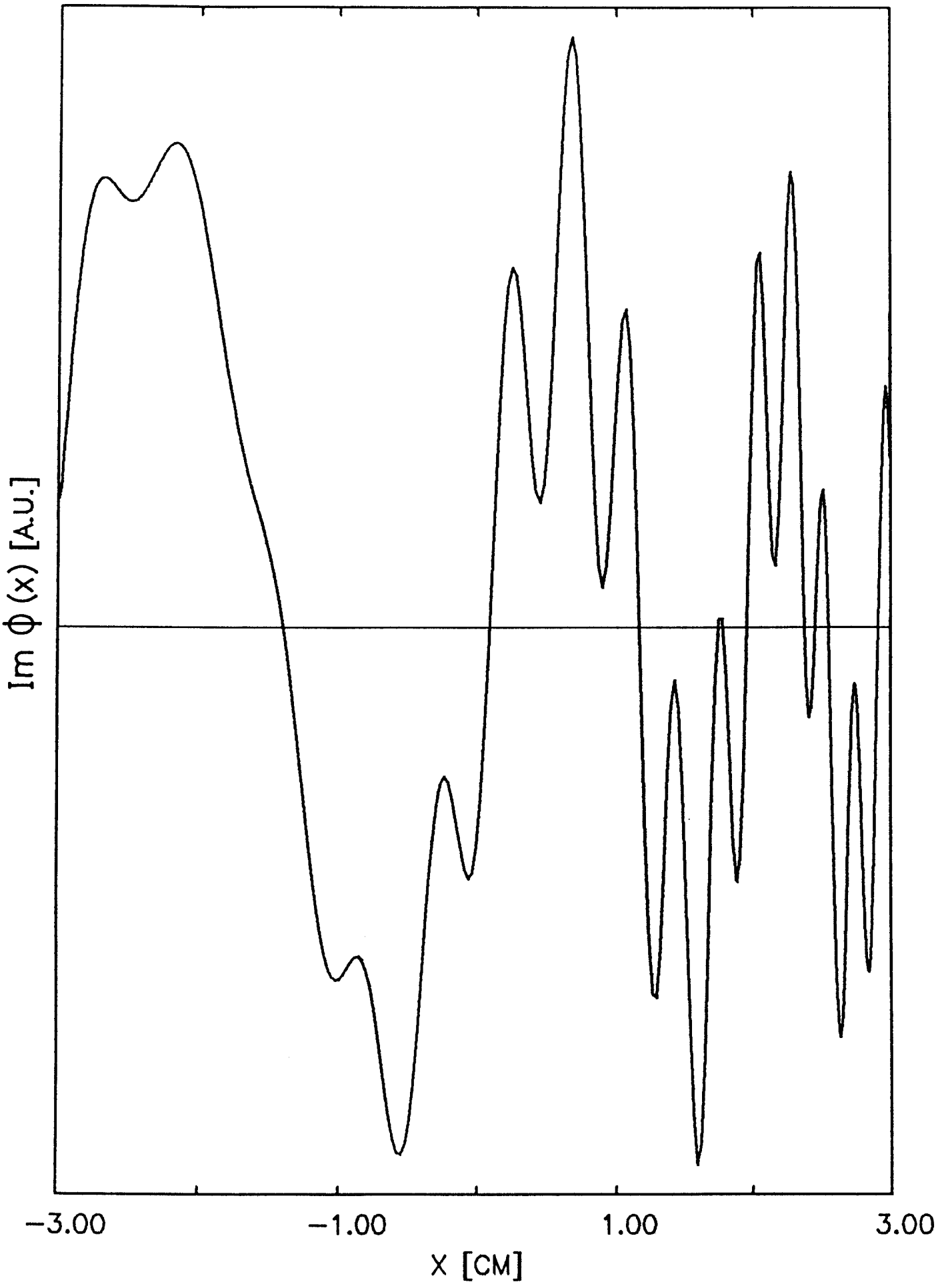

Figure 6.

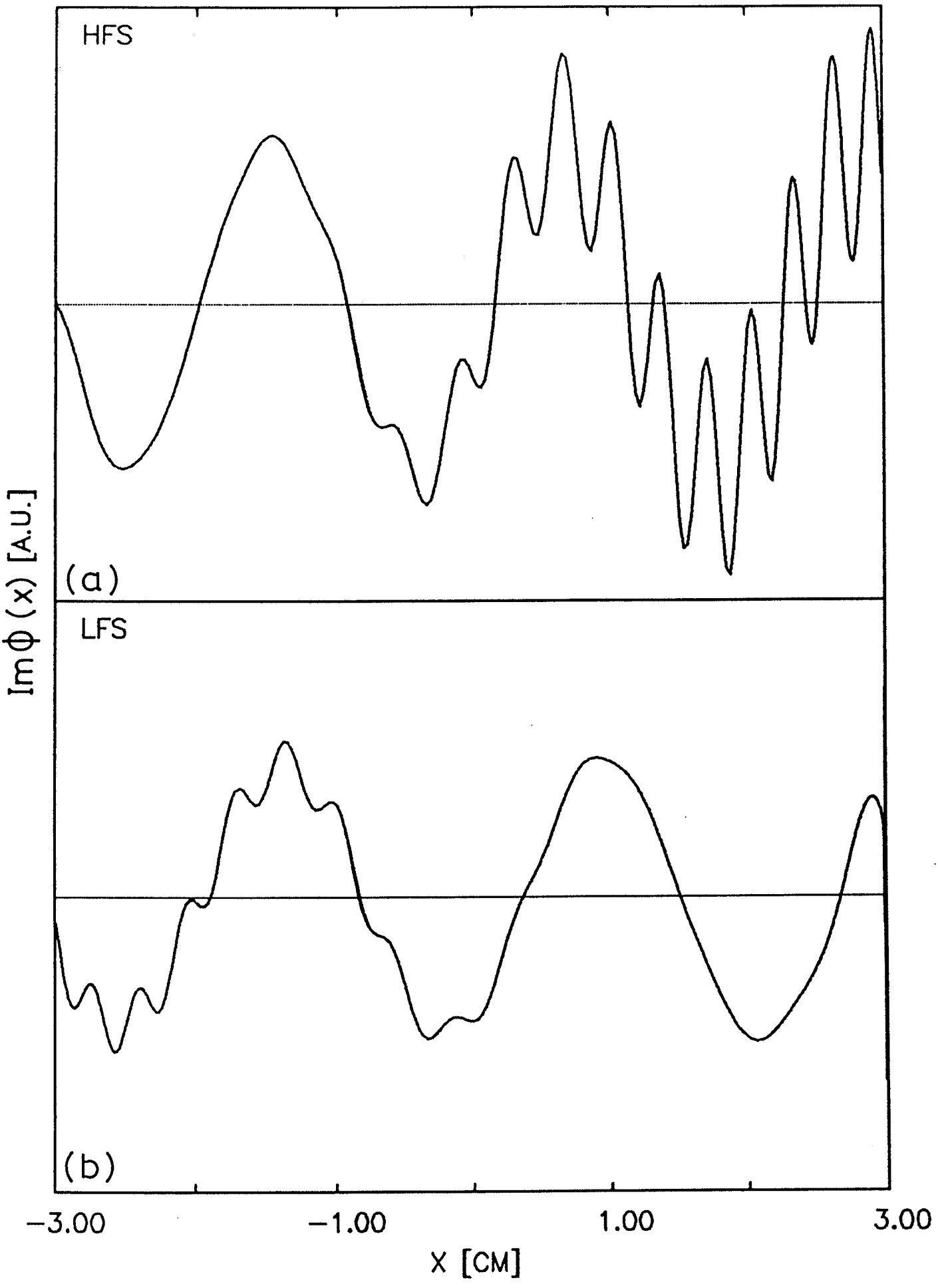

Figure 7.

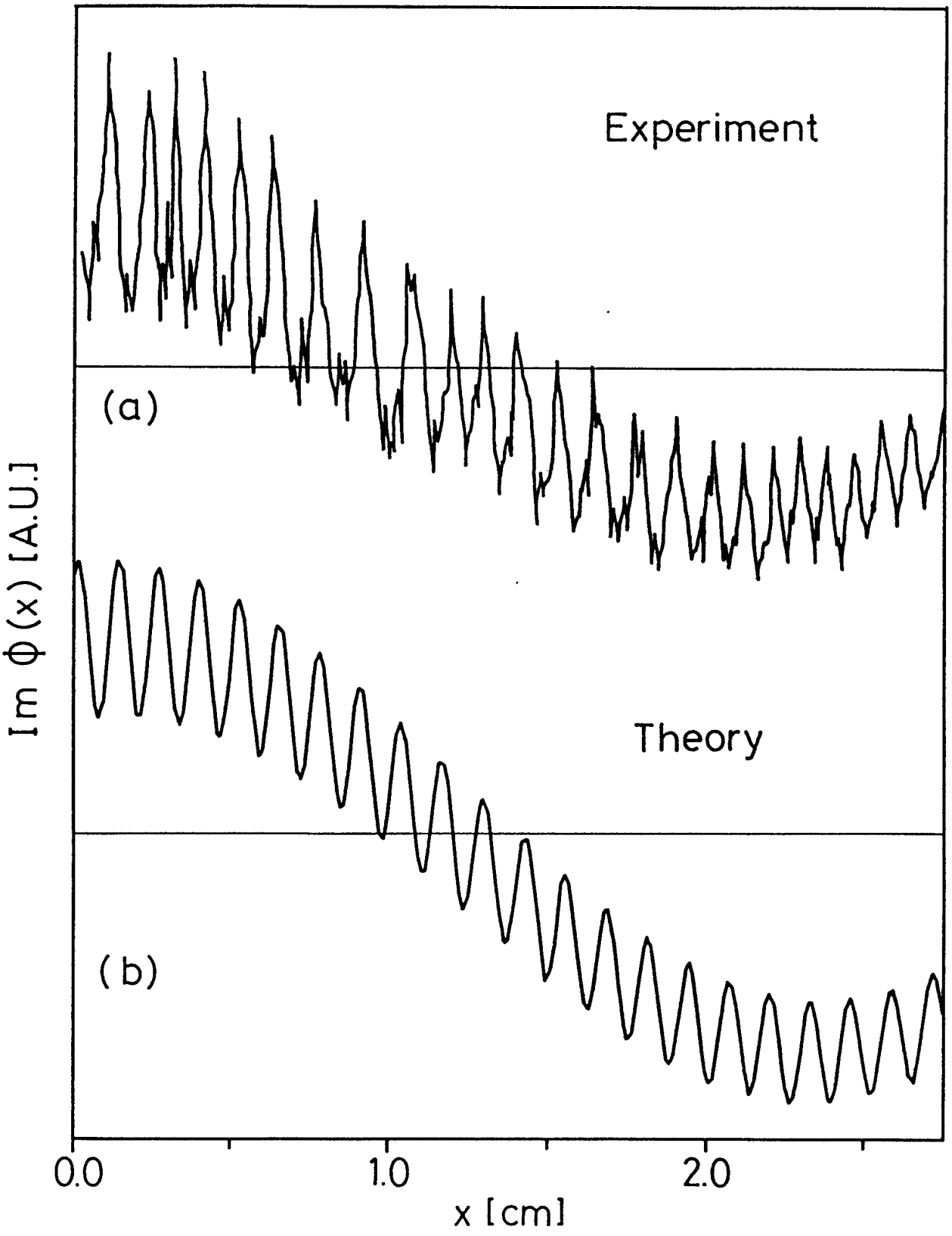

Figure 8.

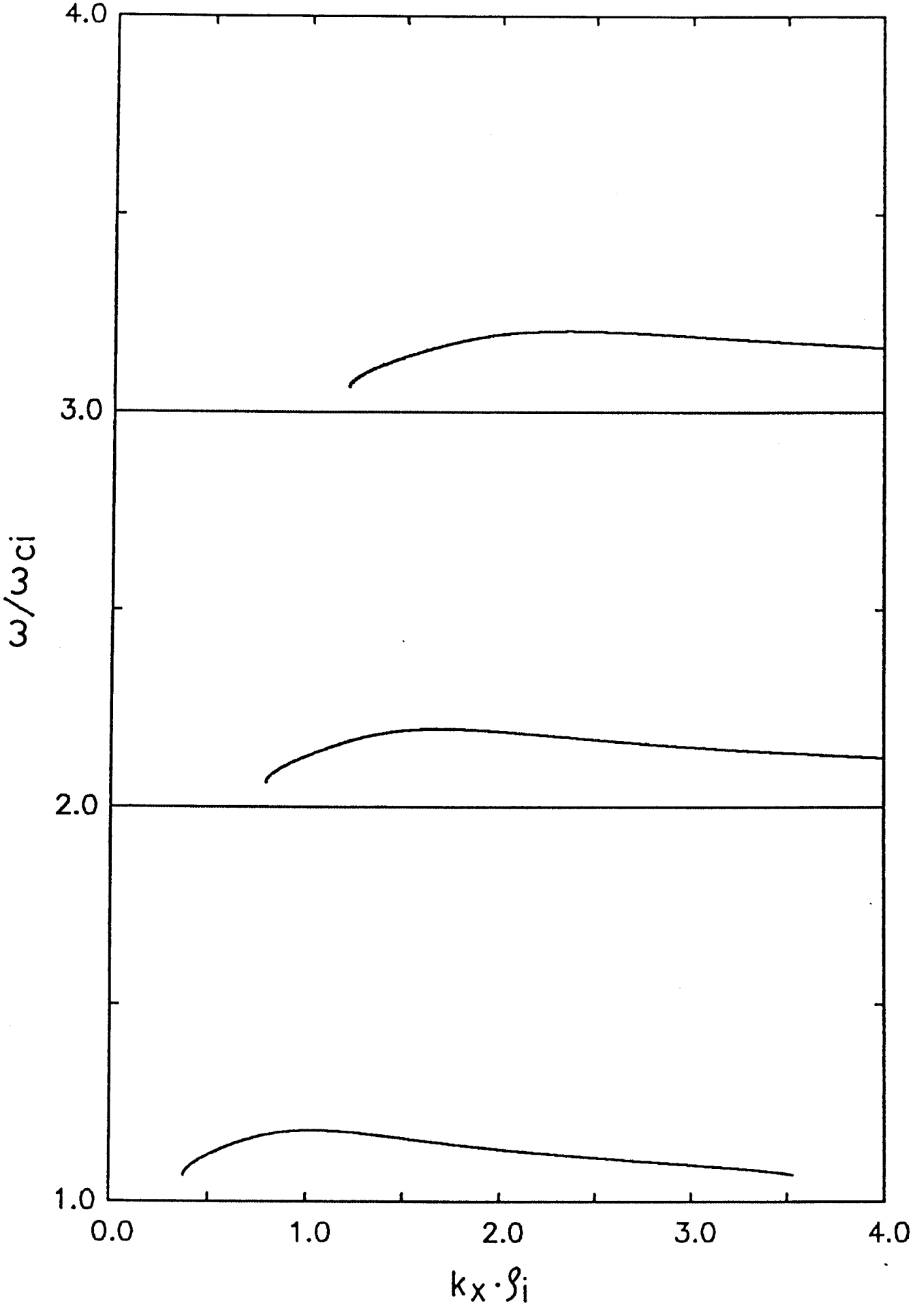

Figure 9.

Figure 10.

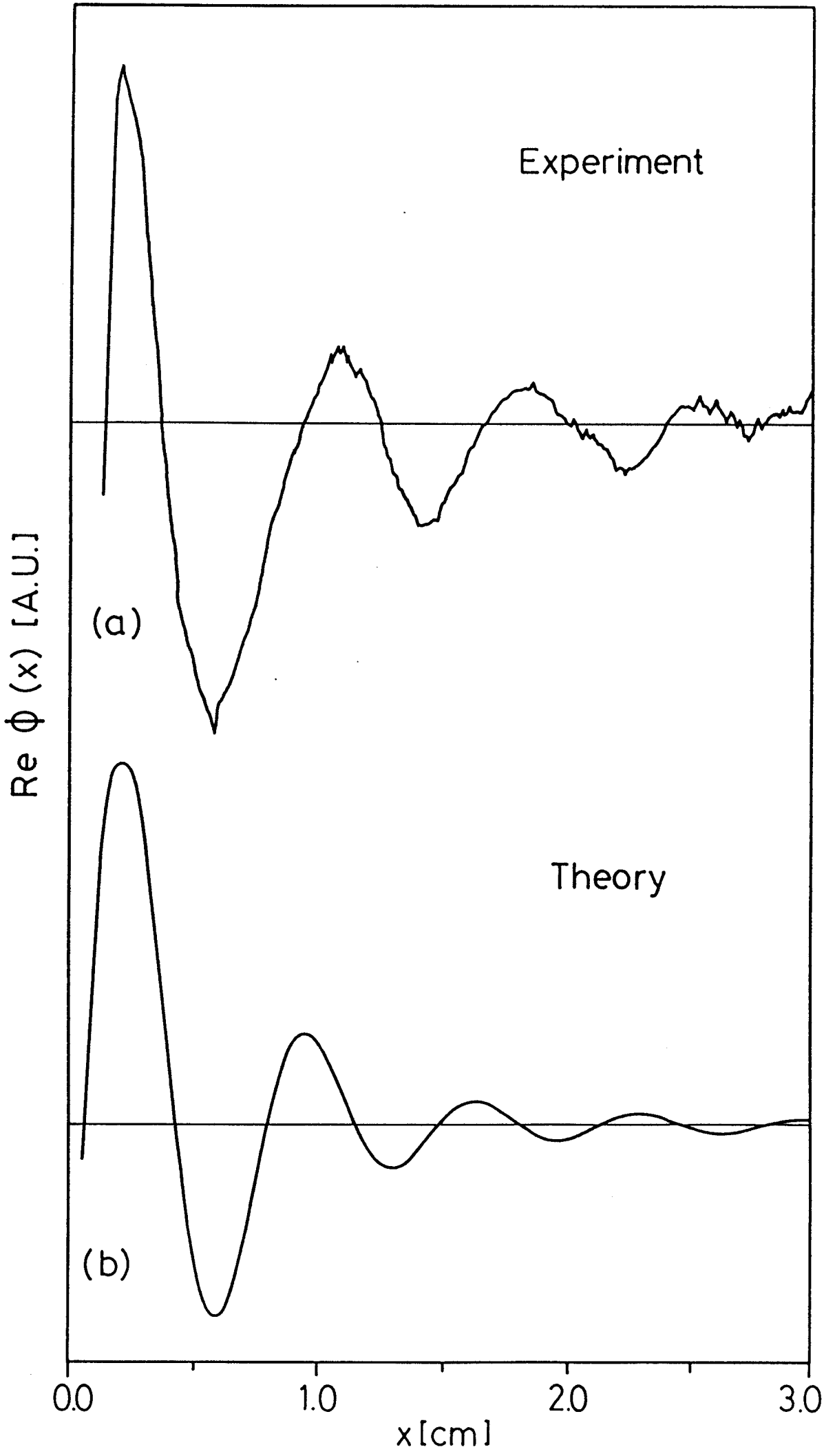

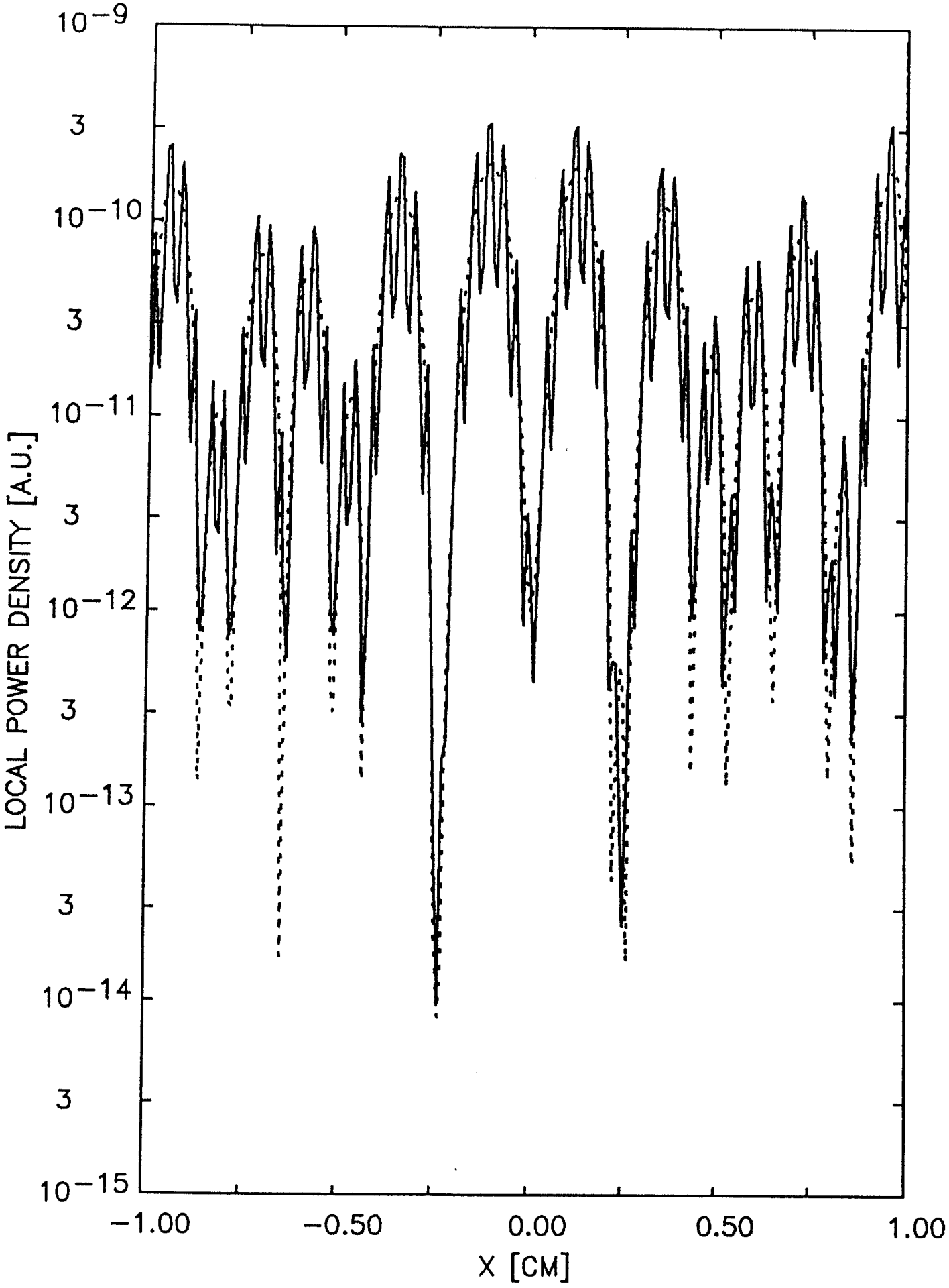
LOCAL POWER DENSITY [A.U.]
10^-9
3
10^-10
3
10^-11
3
10^-12
3
10^-13
3
10^-14
3
10^-15
-1.00
-0.50
0.00
0.50
1.00
X [CM]

Figure 11a.

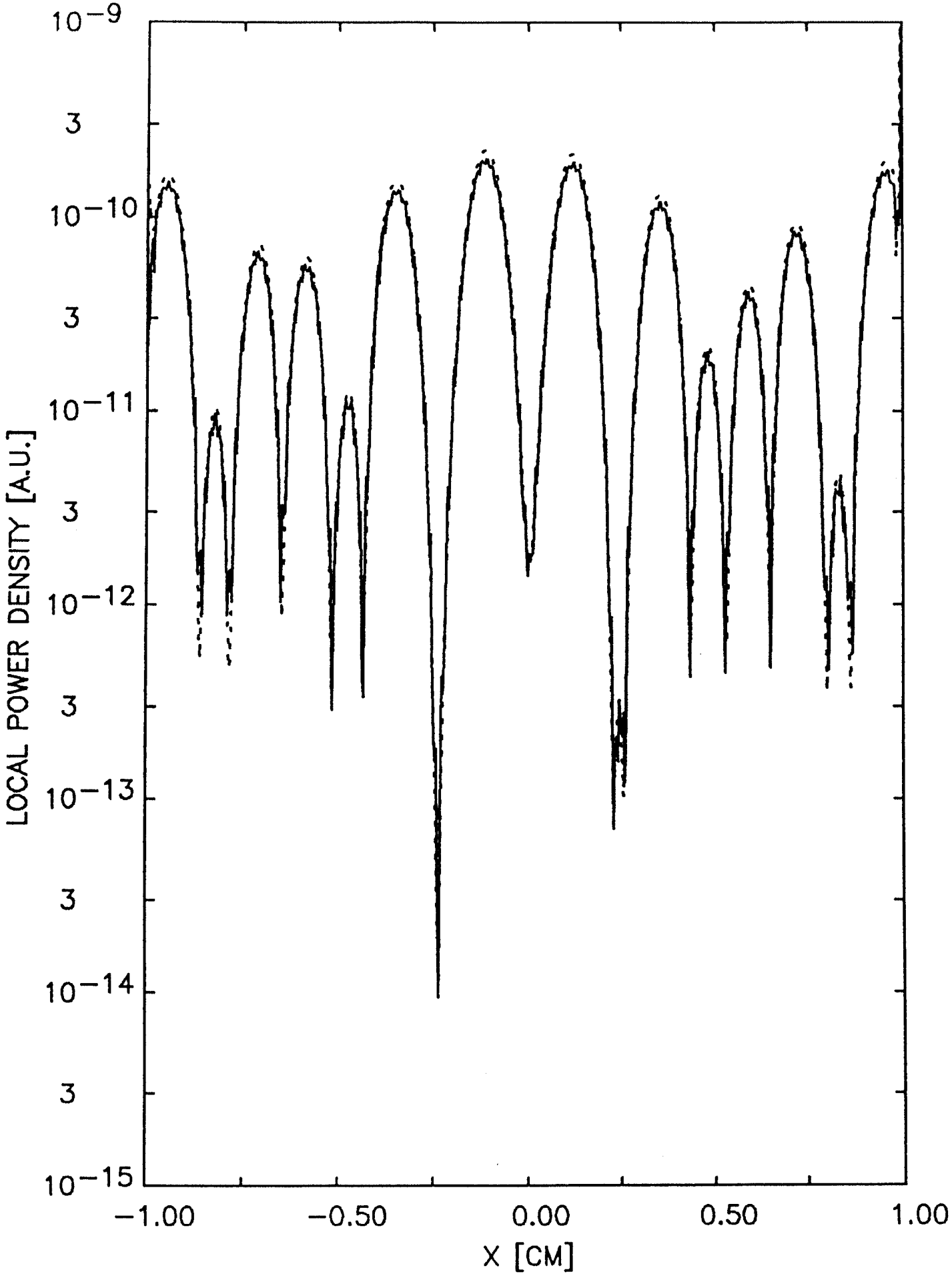
LOCAL POWER DENSITY [A.U.]
10−9
3
10−10
3
10−11
3
10−12
3
10−13
3
10−14
3
10−15
−1.00
−0.50
0.00
0.50
1.00
X [CM]

Figure 11b.

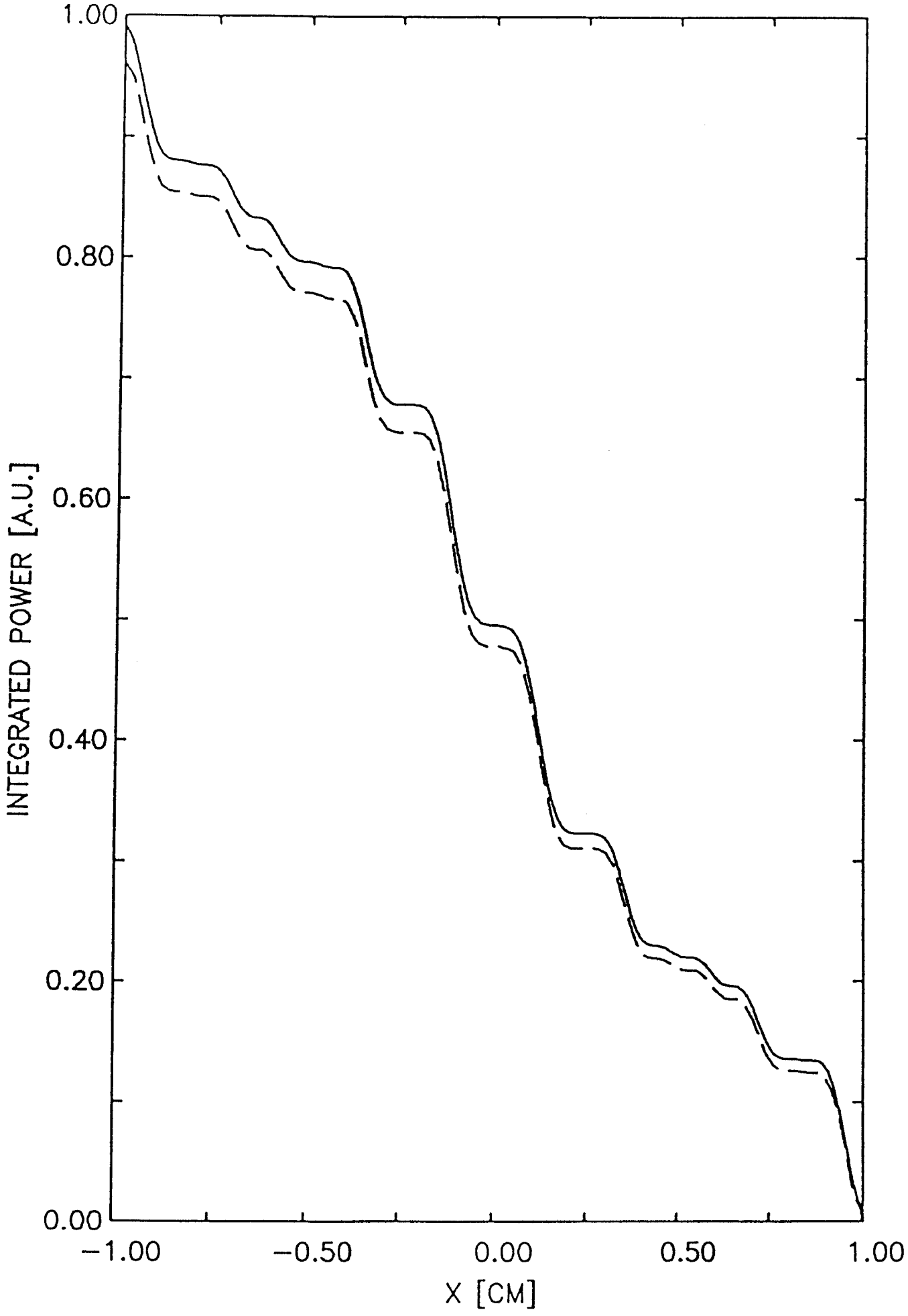
1.00
0.80
0.60
0.40
0.20
0.00
INTEGRATED POWER [A.U.]
−1.00
−0.50
0.00
0.50
1.00
X [CM]

Figure 12a.

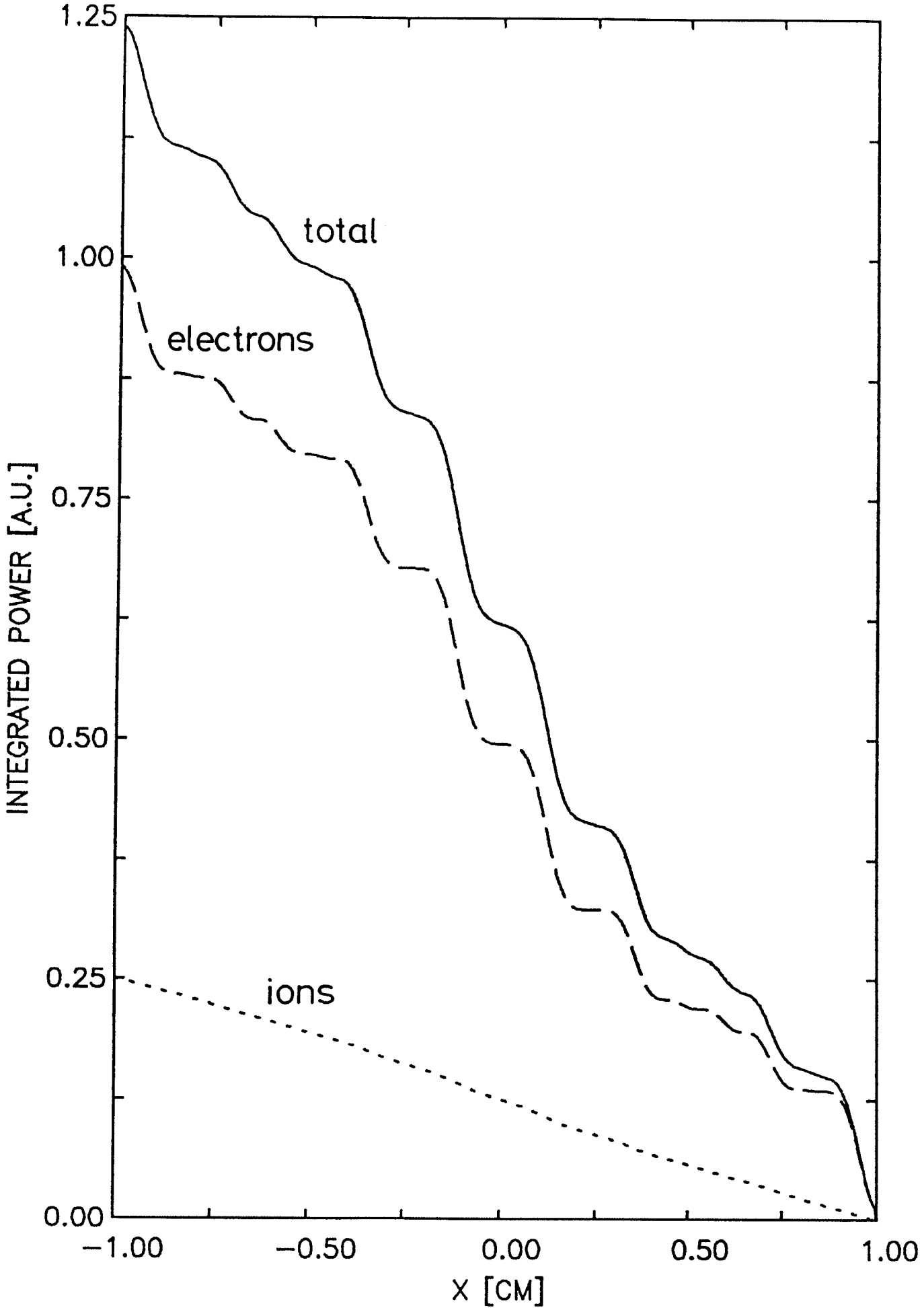
1.25
1.00
0.75
0.50
0.25
0.00
INTEGRATED POWER [A.U.]
total
electrons
ions
−1.00
−0.50
0.00
0.50
1.00
X [CM]

Figure 12b.